Modeling epithelial tissue and cell deformation dynamics using a viscoelastic slab sculpted by surface forces

XinXin Du [*]
Center for Computational Biology, Flatiron Institute, New York, New York 10010, USA

Michael J. Shelley [†]
Center for Computational Biology, Flatiron Institute, New York, New York 10010, USA
and Courant Institute of Mathematical Sciences, New York University, New York, New York 10012, USA

(Received 20 September 2022; accepted 5 May 2023; published 26 June 2023)

During morphogenesis, epithelial monolayers actively alter their shape to create future body parts of the animal; this makes the epithelium one of the most active and critical structures in early animal development. While epithelia are often modeled as two-dimensional systems, real epithelia are not necessarily thin relative to cell cross section, and advances in 3D imaging have shown the possibility of substantial cell deformations in the third dimension, as well as differences in dynamics of the apical and basal surfaces indicative of three-dimensional coupling. With the importance of the third dimension in mind, we have developed a self-sculpting, three-dimensional model of epithelia whose dynamics are driven by active forces on its surface. We present a first, fundamental study for a reduced version of epithelia that investigates how surface forces affect its internal dynamics. Our model captures the 3D slab-like geometry of epithelia, viscoelasticity of tissue response, fluid surroundings, and driving from active surface forces. We represent epithelial tissue as a thick slab, a 3D continuum comprised of a Stokes fluid with an extra viscoelastic stress. Employing this model, we present both analytical and numerical solutions of the system and make quantitative predictions about cell shapes, cell dynamics, and the tissue's response to surface force in a three-dimensional setting. In particular, we investigate the implications of our model on the initiation of ventral furrow invagination and T1 transitions in *Drosophila* embryogenesis. In the former, we demonstrate the importance of fluid and geometric surroundings to drive invagination. In the latter, we show the limitations of surface forces alone to drive T1 transitions.

DOI: 10.1103/PhysRevResearch.5.023190

I. INTRODUCTION

Epithelial cells change shape and rearrange while staying connected in a planar geometry. While many events in morphogenesis, such as tube formation [1] or epithelial invagination [2,3], involve deforming the planar geometry of the epithelium, many of these deformations are preceded by morphological changes in which cells move merely in-plane to the epithelium [4]. Moreover, many events in morphogenesis do not deform the epithelial plane at all, as they consist only of in-plane movement; examples of this include convergent extension in both *Drosophila* [5–7] and vertebrates [8] and ommatidia rotation in *Drosophila* [9].

Whenever epithelial cells move mostly in-plane to the epithelium, researchers often use 2D vertex models [10–14] or particle models [15,16] to describe them. These models are sufficient if the epithelial cells they describe are thin. However, recent developments in microscopy have revealed that when cells have significant height, movements become complex [5], and a three-dimensional approach may be required. To this end, 3D vertex models [17–22] and 3D finite element models [23–25] have been used. While these models have produced effective results to describe both cell rearrangements and tissue deformations, they do not take into account the fluid surroundings of the tissue, nor do they time-evolve internal velocity fields and stresses via momentum balance equations. Moreover, these approaches require many phenomenological parameters to be specified and tuned. The thin viscoelastic shell models of [26,27] treat the mechanics and activities of the actin cortex near cell surfaces as continuum fields and are able to describe in detail the 3D shapes of individual cells; however, the influence of fluid surroundings on the active layer are not modeled. Our approach restricts to modeling phenomena in which cells move mostly in-plane to the epithelium; however, our model epithelium is fully three dimensional, and we consider its interaction with both fluid/material surroundings and boundary constraints.

We present a mathematical model for epithelial tissue in which the tissue is described by a three-dimensional continuum viscoelastic fluid, geometrically, a flat 3D slab, surrounded by viscous fluids. The epithelium is driven by active surface forces, for example, due to populations of actomyosin that exist on the apical or basal surface of cells but not on their lateral sides [28]. One question that our

[*]Corresponding author: xdu@flatironinstitute.org
[†]Corresponding author: mshelley@flatironinstitute.org

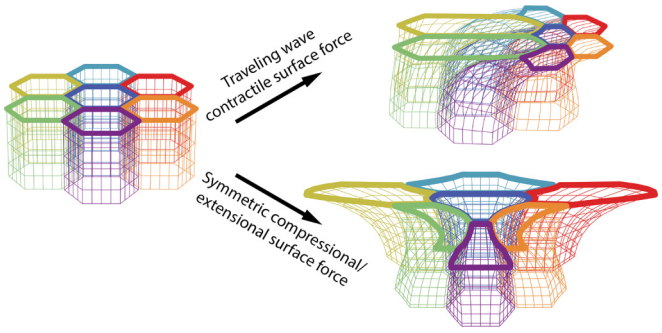

FIG. 1. Simulated 3D cell deformations under two different applied surface forces.

model treats explicitly is how the thickness of the epithelium plays a role in how forces alter cell shape: since forces of contractility are specified only at the surface of the tissue, nonzero thickness means that forces specified on the apical (basal) side do not fully propagate to the basal (apical) side. This would imply that the topology of cells can look different on the apical versus basal surface due to the attenuation of forces through the thickness of the tissue. In fact, research showing that epithelial cells in tissues often have a scutoid shape [29,30] indicates that, indeed, cell topology often differs between apical and basal sides. Our mathematical description quantitatively comments on the nature of force transfer from one side of the epithelium to the other.

Finally, because we model the tissue as a continuum, velocity fields are used to track material elements. If we assume that cell membranes do not exert significant force, that is, that membranes are merely carried by the flow of cytoplasm, shown to be roughly true in the early *Drosophila* embryo [28], then cell boundaries, tracked as material elements, provide simulated data of 3D cell shape change over time. Indeed, authors in [28] found that knocking down lateral membrane formation does not significantly alter the 3D flow inside an embryo, and that tracers of membranes and tracers of the fluid behave similarly; hence ignoring forces from lateral membranes is an appropriate approximation for our zeroth-order model. Figure 1 shows the results of thus simulated 3D cell deformations under different driving surface forces (elaborated in Fig. 7 below). In this paper, we simulate both the onset of ventral furrow invagination and convergent extension in *Drosophila*. We elucidate these events using 3D solutions to the system, accounting for the fluid environment and other geometric constraints.

II. DEFINITION AND SOLUTION TO THE MODEL

A. Biological motivation for model geometry

Biologically and stereotypically, epithelia are flat tissues that, on one side, are separated from a solid-like structure by a layer of fluid, and on the other side, adjacent to a fluidic bath. In the fly embryo, for example, the apical side of the epithelium is located next to the perivitelline fluid layer, which borders the vitelline membrane, while the basal side faces the fluid at the center of the embryo [Fig. 2(a)] [2,3]. We exploit this flat geometry of the epithelium and consider settings where cells move mostly in-plane to the tissue. Moreover,

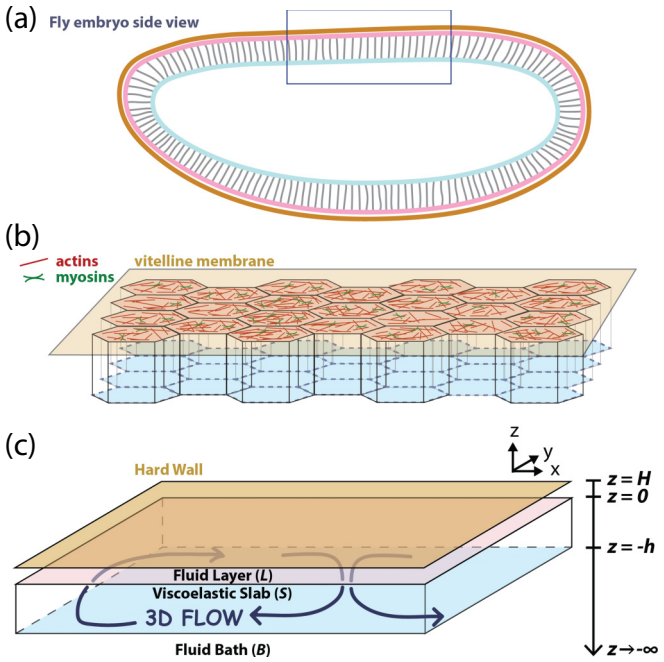

FIG. 2. System geometry. (a) Stereotypical epithelial geometry of the *Drosophila* embryo: one side of the epithelium is adjacent to a fluid layer (perivitelline fluid) and a hard wall (vitelline membrane); the other side faces a fluid bath. The box indicates a region of approximately flat epithelium. (b). Schematic of epithelium with an active surface containing actomyosin adjacent to the perivitelline fluid and vitelline membrane. (c) Diagram of model epithelium with definitions of regions L, S, B, and the coordinate system; the two surfaces of the slab are "top" ($z = 0$) and "bottom" ($z = -h$).

we take into full account the epithelium's interaction in three dimensions with the surrounding fluids and boundaries.

To describe the epithelium mathematically, as a mechanical object, we use a viscoelastic fluid model to represent the epithelium, as researchers [31–33] have found that cells often respond elastically on short timescales and viscously on long timescales. Our length scales and timescales of interest are at the scale of embryonic cell rearrangements, between 1 and 100 microns, and 0.1 to 10 minutes, respectively. Because an epithelium is longer in two directions and shorter in the third, we describe it as a 3D slab that is periodic in the x and y directions with finite thickness h in the z direction. Above the slab, we include a layer of Newtonian fluid (region L), simulating the layer between the epithelium and a solid-like structure, typically a vitelline membrane or extracellular matrix. The solid-like structure itself is represented by a hard wall at $z = H$. The viscoelastic slab occupies the domain $-h \leqslant z \leqslant 0$ (region S). Below the slab, for $z < -h$, we include a fluid bath of infinite depth (region B) to simulate the admittedly finite but large-scale fluidic bath that often exists on the other side of the epithelium. We refer to the side of the slab adjacent to the fluid layer at $z = 0$ as the "top", and the side adjacent to the semi-infinite fluid bath at $z = -h$ as the "bottom". Figure 2(c) shows regions L, S, and B in a schematic diagram.

Active forces are applied along the surface of the slab in the planar directions (x and y). These active forces typically arise from populations of myosin motors moving on an actin mesh

that exists on the surface of the tissue [Fig. 2(b)]. While the forces themselves are two-dimensional, they create a three-dimensional flow inside the tissue because of the internal mechanics of the slab [Fig. 2(c)]. In this paper, we analyze these 3D flows given the particular form of the surface force. Assuming that cell boundaries are carried by the flow, we also characterize cell deformations that arise from this force.

B. The Model

1. Bulk equations

Let the fields $\boldsymbol{\sigma}^L$, $\boldsymbol{\sigma}^S$, and $\boldsymbol{\sigma}^B$ denote the total stress tensors in the L, S, and B regions of the system,

$$\boldsymbol{\sigma}^L \equiv -P^+\mathbb{1} + \eta_L(\boldsymbol{\nabla}\mathbf{u}^+ + (\boldsymbol{\nabla}\mathbf{u}^+)^T), \tag{1}$$

$$\boldsymbol{\sigma}^S \equiv -P\mathbb{1} + \eta(\boldsymbol{\nabla}\mathbf{u} + (\boldsymbol{\nabla}\mathbf{u})^T) + \boldsymbol{\sigma}^e, \tag{2}$$

$$\boldsymbol{\sigma}^B \equiv -P^-\mathbb{1} + \eta_B(\boldsymbol{\nabla}\mathbf{u}^- + (\boldsymbol{\nabla}\mathbf{u}^-)^T), \tag{3}$$

where $\mathbf{u}$, $\mathbf{u}^\pm$ are the velocities, P, $P^\pm$ are the pressures, and η, $\eta_{L,B}$ are the viscosities in each region. Here, $\boldsymbol{\sigma}^{L,B}$ indicate linear Newtonian solvents and $\boldsymbol{\sigma}^e$ indicates an extra stress. We model the tissue as an Oldroyd-B fluid because Oldroyd-B is perhaps the simplest model of a viscoelastic fluid. Requiring

$$\boldsymbol{\nabla}\cdot\boldsymbol{\sigma}^{L,S,B} = 0, \quad \boldsymbol{\nabla}\cdot\mathbf{u} = \boldsymbol{\nabla}\cdot\mathbf{u}^\pm = 0, \tag{4}$$

we obtain the Stokes or forced Stokes equations of motion for fields $\mathbf{u}$, $\mathbf{u}^\pm$, P, $P^\pm$. The extra stress $\boldsymbol{\sigma}^e$ in Eq. (2) is evolved by the equation

$$\overset{\triangledown}{\boldsymbol{\sigma}}^e = D\nabla^2\boldsymbol{\sigma}^e - \frac{1}{\tau_p}(\boldsymbol{\sigma}^e - G_0\mathbb{1}) \tag{5}$$

where

$$\overset{\triangledown}{\boldsymbol{\sigma}}^e = \frac{\partial}{\partial t}\boldsymbol{\sigma}^e + \mathbf{u}\cdot\boldsymbol{\nabla}\boldsymbol{\sigma}^e - (\boldsymbol{\nabla}\mathbf{u}\boldsymbol{\sigma}^e + \boldsymbol{\sigma}^e\boldsymbol{\nabla}\mathbf{u}) \tag{6}$$

is the upper-convected time derivative, and D is the center-of-mass diffusion of Oldroyd-B polymers. Further, recalling the kinetic theory of Oldroyd-B, if we assume that Oldroyd-B particles cannot cross the top or bottom boundaries of the tissue (a natural way to ensure particle number conservation), then this implies that the diffusive flux at $z = 0$ and $z = -h$ are both 0, that is,

$$\frac{\partial}{\partial z}(D\boldsymbol{\sigma}^e)|_{z=0,-h} = \mathbf{0}. \tag{7}$$

To nondimensionalize Eqs. (1)–(5), we rescale time, length, and force as

$$t = t'\tau_p, \quad \ell = \ell'\ell_0, \quad F = F'\eta\frac{\ell_0^2}{\tau_p}, \tag{8}$$

where ℓ_0 is a yet-unspecified characteristic length scale. We additionally rescale $\boldsymbol{\sigma}^e$ by a dimensionless stress α, $\boldsymbol{\sigma}^e = \boldsymbol{\sigma}^{e\prime}\alpha\eta/\tau_p$ where $\alpha\eta/\tau_p = G_0$. We chose dimensional units to depend on the material properties of the system (the solvent viscosity η and polymer relaxation time τ_p), so that parameters specifying the driving force, e.g., its amplitude and frequency, will be free to vary. The details of nondimensionalization are in the Supplemental Material (SM) [34].

Using the scalings in Eq. (8), the nondimensional equations of motion in the fluid layer (region L), the slab (region S), and the fluid bath (region B) are

$$-\boldsymbol{\nabla}P^+ + \eta_L\nabla^2\mathbf{u}^+ = 0, \quad \boldsymbol{\nabla}\cdot\mathbf{u}^+ = 0, \quad 0 < z < H, \tag{9}$$

$$\left.\begin{aligned} -\boldsymbol{\nabla}P + \nabla^2\mathbf{u} + \alpha\boldsymbol{\nabla}\cdot\boldsymbol{\sigma}^e = 0, \quad \boldsymbol{\nabla}\cdot\mathbf{u} = 0 \\ \overset{\triangledown}{\boldsymbol{\sigma}}^e = D\nabla^2\boldsymbol{\sigma}^e - (\boldsymbol{\sigma}^e - \mathbb{1}) \end{aligned}\right\} -h \leqslant z \leqslant 0, \tag{10, 11}$$

$$-\boldsymbol{\nabla}P^- + \eta_B\nabla^2\mathbf{u}^- = 0, \quad \boldsymbol{\nabla}\cdot\mathbf{u}^- = 0, \quad z < -h. \tag{12}$$

2. Boundary conditions

We assume a no-slip condition on the wall,

$$\mathbf{u}^+|_{z=H} = \mathbf{0}. \tag{13}$$

Additionally, we assume that at $z = 0$ and $z = -h$, we have continuity of velocity with a zero-velocity condition in the z direction,

$$\mathbf{u}^+|_{z=0} = \mathbf{u}|_{z=0} = \left(V_x^t, V_y^t, 0\right) \equiv (\mathbf{V}^t, 0), \tag{14}$$

$$\mathbf{u}|_{z=-h} = \mathbf{u}^-|_{z=-h} = \left(V_x^b, V_y^b, 0\right) \equiv (\mathbf{V}^b, 0). \tag{15}$$

Here, the planar (x, y) velocity at $z = 0$ is denoted $\mathbf{V}^t \equiv (V_x^t, V_y^t)$ where the superscript denotes the "top" surface of the slab, and the planar velocity at $z = -h$ is denoted $\mathbf{V}^b \equiv (V_x^b, V_y^b)$ where the superscript denotes the "bottom" surface of the slab. We also demand that velocities at $-\infty$ vanish,

$$\mathbf{u}^-|_{z\to-\infty} = \mathbf{0}. \tag{16}$$

Finally, we have boundary conditions reflecting the fact that actively applied tangential forces at the top ($z = 0$) and bottom ($z = -h$) surfaces of the slab create stress jumps across those surfaces. Let $\mathbf{F}^t$ and $\mathbf{F}^b$ notate stresses from active driving forces applied at the top and bottom surfaces, respectively. Then

$$(\boldsymbol{\sigma}^S - \boldsymbol{\sigma}^L)\hat{\mathbf{z}}|_{z=0,2\mathrm{D}} = \mathbf{F}^t, \tag{17}$$

$$(\boldsymbol{\sigma}^B - \boldsymbol{\sigma}^S)\hat{\mathbf{z}}|_{z=-h,2\mathrm{D}} = \mathbf{F}^b, \tag{18}$$

where the notation $|_{z=z_0,2\mathrm{D}}$ is defined by $\mathbf{v}|_{z=z_0,2\mathrm{D}} \equiv (v_x, v_y)|_{z=z_0}$ for an arbitrary 3D vector $\mathbf{v} = (v_x, v_y, v_z)$. The z-directional stress at the top and bottom surfaces are determined by the condition that $w = 0$ at $z = 0, -h$.

C. Fourier representation of solution when $\sigma^e = 0$: The Stokes solution

If we assume that the slab is a simple Stokes fluid, setting $\boldsymbol{\sigma}^e = \mathbf{0}$ in Eq. (10) and eliminating Eq. (11) entirely, then the velocity field can be determined everywhere in the system as a nonlocal functional of the surface forces [35]. This involves solving a Neumann-to-Dirichlet mapping from surface forces to surface velocities. We Fourier transform the Stokes equations in x and y. Stress boundary conditions are applied to 3D velocity solutions such that the surface forces $\mathbf{F}^t$ and $\mathbf{F}^b$ self-consistently determine the surface velocities $\mathbf{V}^t$ and $\mathbf{V}^b$ through a Neumann-to-Dirichlet map.

A 2D Fourier transform of an arbitrary scalar function f is defined as

$$f(\mathbf{x}) = \sum_{i,j} \tilde{f}(k_i, k_j, z) e^{i(k_i,k_j)\cdot(x,y)} \equiv \sum_{\mathbf{k}} \tilde{f}(\mathbf{k}, z) e^{i\mathbf{k}\cdot\mathbf{x}} \quad (19)$$

where $\mathbf{k}$ takes on values

$$\mathbf{k} \equiv \left(\frac{2\pi i}{L}, \frac{2\pi j}{L}\right), \quad i, j \in \mathbb{Z}. \quad (20)$$

We notate $\tilde{\mathbf{u}} = (\tilde{u}_x, \tilde{u}_y, \tilde{u}_z) \equiv (\tilde{\mathbf{v}}, \tilde{w})$ so that $\tilde{\mathbf{v}} = (\tilde{u}_x, \tilde{u}_y)$. Using Eq. (19) to Fourier transform all fields in the Stokes equation $0 = -\nabla P + \eta\nabla^2\mathbf{u}$ and applying the divergence-less condition $\nabla \cdot \mathbf{u} = 0$ leads to the 2D transformed Stokes equations and divergenceless condition

$$-i\mathbf{k}\tilde{P} + \eta\left(-k^2 + \frac{\partial^2}{\partial z^2}\right)\tilde{\mathbf{v}} = 0, \quad (21)$$

$$-\frac{d}{dz}\tilde{P} + \eta\left(-k^2 + \frac{\partial^2}{\partial z^2}\right)\tilde{w} = 0, \quad (22)$$

$$i\mathbf{k}\cdot\tilde{\mathbf{v}} + \frac{\partial}{\partial z}\tilde{w} = 0, \quad (23)$$

where all fields are functions of $(\mathbf{k}, z)$ and $k \equiv |\mathbf{k}|$. The boundary conditions for $\hat{\mathbf{v}}$ and $\hat{w}$, from Eqs. (14) and (15), are

$$\tilde{\mathbf{v}}|_{z=0} = \tilde{\mathbf{V}}^t, \quad \tilde{w}|_{z=0} = 0, \quad (24)$$

$$\tilde{\mathbf{v}}|_{z=-h} = \tilde{\mathbf{V}}^b, \quad \tilde{w}|_{z=-h} = 0. \quad (25)$$

Solutions for Eqs. (21)–(23) are presented in Sec. SII A of the SM [34].

D. Neumann-to-Dirichlet map of surface forces to surface velocities

The full 3D velocity solutions $\tilde{\mathbf{v}}$ and $\tilde{w}$ to the divergenceless Stokes equations [Eqs. (21)–(23)] in the bulk of the tissue are given in the SM [34] by Eqs. (S30) and (S26). Importantly, since Stokes equations are boundary value problems, these bulk velocities are determined by, and are functionals of, the surface velocities $\tilde{\mathbf{V}}^{t,b}$. This dependence means that tangential shear stresses $\mathbf{s}_S^t$ and $\mathbf{s}_S^b$ at the boundaries $z = 0$ and $z = -h$, created by bulk velocities in region S, also depend on $\tilde{\mathbf{V}}^{t,b}$; similarly, the same dependence applies to tangential shear stresses at $z = 0, -h$ created by bulk velocities in regions L and B. The dependence of shear stresses on boundary velocities gives rise to a mathematical opportunity, in which demanding self-consistency between active force and shear stress differences across surfaces allows for the calculation of surface velocities $\tilde{\mathbf{V}}^{t,b}$ as a function of the active surface force. This *Neumann-to-Dirichlet map* between surface force and surface velocity does not only provide the mathematical solution to our posed problem, but is also interpreted as the tissue's velocity response to driving. To see this, consider the following. The tangential shear stresses $\mathbf{s}_S^t$ and $\mathbf{s}_S^b$ at the boundaries $z = 0$ and $z = -h$ from velocities in region S are (see details in the SM [34])

$$\begin{aligned}\boldsymbol{\sigma}^S\hat{\mathbf{z}}|_{z=0,2\mathrm{D}} &\equiv \mathbf{s}_S^t = \boldsymbol{\Theta}_1(k,h,\eta)\tilde{\mathbf{V}}^t - \boldsymbol{\Theta}_2(k,h,\eta)\tilde{\mathbf{V}}^b,\\ \boldsymbol{\sigma}^S\hat{\mathbf{z}}|_{z=-h,2\mathrm{D}} &\equiv \mathbf{s}_S^b = \boldsymbol{\Theta}_2(k,h,\eta)\tilde{\mathbf{V}}^t - \boldsymbol{\Theta}_1(k,h,\eta)\tilde{\mathbf{V}}^b,\end{aligned} \quad (26)$$

where the matrix operators $\boldsymbol{\Theta}_1$ and $\boldsymbol{\Theta}_2$ (given in Eq. S49 in the SM [34]) acting on $\tilde{\mathbf{V}}^t$ and $\tilde{\mathbf{V}}^b$ depend on the magnitude of the wavevector k and parameters h and η (rescaled to 1 from nondimensionalization but reinstated here for clarity). A similar calculation in the SM [34] gives, for tangential shear stresses from regions L and B,

$$\boldsymbol{\sigma}^L\hat{\mathbf{z}}|_{z=0,2\mathrm{D}} \equiv \mathbf{s}_L = -\boldsymbol{\Lambda}(k,H,\eta_L)\tilde{\mathbf{V}}^t, \quad (27)$$

$$\boldsymbol{\sigma}^B\hat{\mathbf{z}}|_{z=-h,2\mathrm{D}} \equiv \mathbf{s}_B = \boldsymbol{\beta}(k,\eta_B)\tilde{\mathbf{V}}^b, \quad (28)$$

where the matrix operators $\boldsymbol{\Lambda}$ and $\boldsymbol{\beta}$ are given in Eqs. (S51) and (S52) (see SM [34]). Assuming that the stress jumps at $z = 0$ and $z = -h$ are created by active forces $\mathbf{F}^t$ and $\mathbf{F}^b$, respectively, we obtain

$$\mathbf{s}_S^t - \mathbf{s}_L = \tilde{\mathbf{F}}^t, \quad (29)$$

$$\mathbf{s}_B - \mathbf{s}_S^b = \tilde{\mathbf{F}}^b. \quad (30)$$

Inverting these equations, we express $\tilde{\mathbf{V}}^t$ and $\tilde{\mathbf{V}}^b$ in terms of $\tilde{\mathbf{F}}^t$ and $\tilde{\mathbf{F}}^b$,

$$\tilde{\mathbf{V}}^t = -\left(\boldsymbol{\Theta}_2 - \boldsymbol{\Gamma}_B\boldsymbol{\Theta}_2^{-1}\boldsymbol{\Gamma}_L\right)^{-1}\left(\tilde{\mathbf{F}}^b + \boldsymbol{\Gamma}_B\boldsymbol{\Theta}_2^{-1}\tilde{\mathbf{F}}^t\right) \equiv \boldsymbol{\tau}\tilde{\mathbf{F}}^b + \boldsymbol{\tau}^t\tilde{\mathbf{F}}^t \quad (31)$$

$$\tilde{\mathbf{V}}^b = -\left(\boldsymbol{\Theta}_2 - \boldsymbol{\Gamma}_L\boldsymbol{\Theta}_2^{-1}\boldsymbol{\Gamma}_B\right)^{-1}\left(\tilde{\mathbf{F}}^t + \boldsymbol{\Gamma}_L\boldsymbol{\Theta}_2^{-1}\tilde{\mathbf{F}}^b\right) \equiv \boldsymbol{\tau}\tilde{\mathbf{F}}^t + \boldsymbol{\tau}^b\tilde{\mathbf{F}}^b \quad (32)$$

where $\boldsymbol{\Gamma}_B \equiv \boldsymbol{\Theta}_1 + \boldsymbol{\beta}$ and $\boldsymbol{\Gamma}_L \equiv \boldsymbol{\Theta}_1 + \boldsymbol{\Lambda}$. Note that the matrices $\boldsymbol{\Theta}_{1,2}$, $\boldsymbol{\Gamma}_{L,B}$, $\boldsymbol{\beta}$, $\boldsymbol{\Lambda}$, all have the form $p(k)\mathbb{1} + q(k)\hat{\mathbf{k}}\hat{\mathbf{k}}$ where $p \neq 0$ and $q \neq -p$. Hence each is invertible with its inverse of the form $\frac{1}{p}(\mathbb{1} - \frac{q}{p+q}\hat{\mathbf{k}}\hat{\mathbf{k}})$ where $(\hat{\mathbf{k}}\hat{\mathbf{k}})_{ij} \equiv k_ik_j/k^2$; additionally, they all commute under multiplication. Hence, the same matrix $\boldsymbol{\tau}$ multiplies $\tilde{\mathbf{F}}^b$ in Eq. (31) and $\tilde{\mathbf{F}}^t$ in Eq. (32), meaning that the transfer of surface forces to velocities on opposite surfaces are identical regardless of direction of transfer. Further, the transfer matrices $\boldsymbol{\tau}$, $\boldsymbol{\tau}^{t,b}$, like the other matrices in this discussion, are also nonsingular rank-one perturbations of the identity. Thus, we have determined $\mathbf{V}^{t,b}$ as functionals of surface forces $\mathbf{F}^{t,b}$. Finally, Eqs. (S26), (S28), (S30), (S44)–(S46), and (S39)–(S41) (see SM [34]) give the bulk velocities $\mathbf{u}$, $\mathbf{u}^{\pm}$ and pressures P, $P^{\pm}$ in terms of $\mathbf{V}^{t,b}$.

E. Stokes Oldroyd-B solution

To construct the full solution to the Stokes Oldroyd-B equation [Eq. (10)] in region S, we need to consider the source term $\alpha\nabla\cdot\boldsymbol{\sigma}^e$. We first construct, numerically, a particular solution to Eq. (10) using zero velocity boundary conditions at $z = -h, 0$. We add to this a homogenous solution (as in the previous section) that corrects the boundary conditions and so obtain the full solution. This is detailed in Sec. SIII of the SM [34]. The end result is that the quantities

$$\tilde{\mathbf{F}}^t_{\mathrm{OB}} = \tilde{\mathbf{F}}^t - (\boldsymbol{\sigma}_N(P_p, \mathbf{u}_p, \eta) + \alpha\boldsymbol{\sigma}^e)\hat{\mathbf{z}}|_{z=0,2\mathrm{D}}, \quad (33)$$

$$\tilde{\mathbf{F}}^b_{\mathrm{OB}} = \tilde{\mathbf{F}}^b + (\boldsymbol{\sigma}_N(P_p, \mathbf{u}_p, \eta) + \alpha\boldsymbol{\sigma}^e)\hat{\mathbf{z}}|_{z=-h,2\mathrm{D}}, \quad (34)$$

are substituted for $\tilde{\mathbf{F}}^t$ and $\tilde{\mathbf{F}}^b$ to find velocities $\tilde{\mathbf{V}}^t$ and $\tilde{\mathbf{V}}^b$ in Eqs. (31) and (32). In the above, $\mathbf{u}_p$ and P_p indicate the numerical particular solution and $\boldsymbol{\sigma}_N(P, \mathbf{u}, \eta) \equiv -P\mathbb{1} + \eta(\nabla\mathbf{u} + (\nabla\mathbf{u})^T)$. Explicitly, we have

$$\tilde{\mathbf{V}}^t = -\left(\boldsymbol{\Theta}_2 - \boldsymbol{\Gamma}_B\boldsymbol{\Theta}_2^{-1}\boldsymbol{\Gamma}_L\right)^{-1}\left(\tilde{\mathbf{F}}^b_{\mathrm{OB}} + \boldsymbol{\Gamma}_B\boldsymbol{\Theta}_2^{-1}\tilde{\mathbf{F}}^t_{\mathrm{OB}}\right), \quad (35)$$

$$\tilde{\mathbf{V}}^b = -\left(\boldsymbol{\Theta}_2 - \boldsymbol{\Gamma}_L\boldsymbol{\Theta}_2^{-1}\boldsymbol{\Gamma}_B\right)^{-1}\left(\tilde{\mathbf{F}}^t_{\mathrm{OB}} + \boldsymbol{\Gamma}_L\boldsymbol{\Theta}_2^{-1}\tilde{\mathbf{F}}^b_{\mathrm{OB}}\right). \quad (36)$$

Quantities $\mathbf{F}^t_{\rm OB}$ and $\mathbf{F}^b_{\rm OB}$ now include active forces $\mathbf{F}^t$ and $\mathbf{F}^b$ as well induced forces from the extra stress and the particular solution in the slab. As before, these $\hat{\mathbf{V}}^t$ and $\hat{\mathbf{V}}^b$ are utilized in Eqs. (S26), (S28), (S30), (S44)–(S46), and (S39)–(S41) (see SM [34]) to obtain $\mathbf{u}_h$, $\mathbf{u}^{\pm}$, P_h, $P^{\pm}$. These, along with numerical solutions P_p and $\mathbf{u}_p$ give the solution for the full system. Note that since the velocity boundary conditions for P_p and $\mathbf{u}_p$ are $\mathbf{0}$, then Eqs. (35) and (36) indicate the entirety of the surface velocities.

III. THE TRANSFER MATRICES

A. Dependencies on wavevector and other parameters

To understand how the geometry (parameters h and H) and intensive material parameters (viscosities $\eta_{B,L}$) influence how surface force is converted to surface velocities, we explore how transfer matrices depend on the wavevector $\mathbf{k}$, the thickness of the slab h, and other parameters. Consider Eqs. (31) and (32). Note that each of $\boldsymbol{\tau}$, $\boldsymbol{\tau}^t$, and $\boldsymbol{\tau}^b$ have the form

$$\boldsymbol{\tau}(\mathbf{k}) = a(k)\mathbb{1} + b(k)\hat{\mathbf{k}}\hat{\mathbf{k}}, \quad \boldsymbol{\tau}^{t,b} = a^{t,b}(k)\mathbb{1} + b^{t,b}(k)\hat{\mathbf{k}}\hat{\mathbf{k}}. \tag{37}$$

From Eq. (37), the eigenvalues and corresponding eigenvectors of $\boldsymbol{\tau}$ are $e_1 = a(k) + b(k)$, $\mathbf{v}_1 = \hat{\mathbf{k}}$ and $e_2 = a(k)$, $\mathbf{v}_2 = \hat{\mathbf{k}}^{\perp} \equiv (-k_y, k_x)/k$. Analogous eigenvectors and eigenvalues hold for $\boldsymbol{\tau}^{t,b}$. Using the eigenvectors of $\boldsymbol{\tau}$, we express the action of $\boldsymbol{\tau}$ on an arbitrary vector $\tilde{\mathbf{F}} = (\tilde{F}_x(\mathbf{k}), \tilde{F}_y(\mathbf{k}))$ in the basis of vectors parallel and perpendicular to $\tilde{\mathbf{F}}$, vectors $\tilde{\mathbf{F}}$ and $\tilde{\mathbf{F}}^{\perp}$,

$$\boldsymbol{\tau}\tilde{\mathbf{F}} = (a(k) + (\hat{\tilde{\mathbf{F}}} \cdot \hat{\mathbf{k}})^2 b(k))\tilde{\mathbf{F}} + (-(\hat{\tilde{\mathbf{F}}} \cdot \hat{\mathbf{k}})(\hat{\tilde{\mathbf{F}}} \cdot \hat{\mathbf{k}}^{\perp})b(k))\tilde{\mathbf{F}}^{\perp}. \tag{38}$$

Equation (38) is derived in Sec. SIV A of the SM [34]. Interpreting $\tilde{\mathbf{F}}$ as the $\mathbf{k}$th Fourier component of a driving force profile $\mathbf{F}(x, y)$, Eq. (38) indicates that the action of $\boldsymbol{\tau}$ on $\tilde{\mathbf{F}}$, which produces a surface velocity, is proportional to $|\tilde{\mathbf{F}}|$ (as it should) and depends strongly and explicitly on the orientation of wavevector $\mathbf{k}$ with respect to the orientation of the driving force, evident from the factors $\hat{\tilde{\mathbf{F}}} \cdot \hat{\mathbf{k}}$ and $\hat{\tilde{\mathbf{F}}} \cdot \hat{\mathbf{k}}^{\perp}$. We take $\tilde{\mathbf{F}}$ to be in the x direction, i.e., $\tilde{\mathbf{F}} = (\tilde{F}_x, 0)$, then Eq. (38) becomes

$$\begin{aligned}\boldsymbol{\tau}\tilde{\mathbf{F}} &= \left[\left(a(k) + \frac{k_x^2}{k^2}b(k)\right)\hat{\mathbf{x}} + \left(\frac{k_x k_y}{k^2}b(k)\right)\hat{\mathbf{y}}\right]\tilde{F}_x \\ &\equiv (\tau_{\parallel}(\mathbf{k})\hat{\mathbf{x}} + \tau_{\perp}(\mathbf{k})\hat{\mathbf{y}})\,\tilde{F}_x.\end{aligned} \tag{39}$$

Here, we defined the coefficient of force in the x direction as the "parallel transfer coefficient" $\tau_{\parallel}$ and the coefficient of force in the y direction as the "perpendicular transfer coefficient" $\tau_{\perp}$. We assume the driving force $\hat{\tilde{\mathbf{F}}}$ is aligned along x for the rest of the paper and take k_x and k_y to be positive.

Transfer functions $\boldsymbol{\tau}^t$ and $\boldsymbol{\tau}^b$ generate similar expressions to Eq. (39),

$$\begin{aligned}\boldsymbol{\tau}^{t,b}\tilde{\mathbf{F}} &= \left[\left(a^{t,b}(k) + \frac{k_x^2}{k^2}b^{t,b}(k)\right)\hat{\mathbf{x}} + \left(\frac{k_x k_y}{k^2}b^{t,b}(k)\right)\hat{\mathbf{y}}\right]\tilde{F}_x \\ &\equiv (\tau^{t,b}_{\parallel}(\mathbf{k})\hat{\mathbf{x}} + \tau^{t,b}_{\perp}(\mathbf{k})\hat{\mathbf{y}})\,\tilde{F}_x.\end{aligned} \tag{40}$$

From Eqs. (39) and (40), it is evident that the force profile must vary in both x and y to produce a velocity perpendicular to the force. For example, a force profile $F_x(x, y) = \sin(k_x x)$ or $F_x(x, y) = \sin(k_y y)$ will produce no y velocity.

We explore how a, b and $a^{t,b}$, $b^{t,b}$ behave as k and other physical parameters are varied, and then comment on the consequences for parallel and perpendicular transfer coefficients $\tau_{\parallel}$, $\tau_{\perp}$, $\tau^{t,b}_{\parallel}$, $\tau^{t,b}_{\perp}$.

Figure 3 shows $a(k), a^{t,b}(k)$ (shades of red) and $b(k), b^{t,b}(k)$ (shades of brown) as functions of k using the dimensionless (rescaled using η and ℓ_0) base parameters $\eta_B = \eta_L = 1, H = 0.5, h = 2, L = 20$. Here, each graph varies one of the parameters h, H, η_B, or η_L higher or lower by numerical factors and plots the result in a lighter or darker shade, respectively. The range between which each of these parameters approaches 0 and ∞ are shaded. The base parameters are chosen to mimic physical parameters in the fly embryo, where, if the length scale ℓ_0, is taken as the radius of a typical cell, then the thickness of the fluid layer H is typically $0.1\ell_0$ to $2\ell_0$, the thickness of the epithelium h is typically $0.5\ell_0$ to $10\ell_0$, and the viscosities of the fluid bath and fluid layer (η_B and η_L) are on the order of η. Figure S1 (see SM [34]) shows the same functions considered as functions of h using the same base parameters as Fig. 3.

From Figs. 3 and S1 (see SM [34]) and analysis, we make several observations about the behavior of the matrix elements a, b and $a^{t,b}, b^{t,b}$ of the transfer matrices $\boldsymbol{\tau}$ and $\boldsymbol{\tau}^{t,b}$. Elaborations on these points and other comments appear in Sec. SIV B of the SM [34]. (1) We note that perpendicular transfer coefficients $\tau_{\perp}$, $\tau^{t,b}_{\perp}$ are *always* negative; this is due to the quantities $b, b^{t,b}$ being negative, see Figs. 3 and S1 and Secs, SIV C and SIV B (see SM [34]). This means that if the surface force is compressional (extensional) in the x direction, then the velocity produced on *any* surface in the y direction will *always* be extensional (compressional). (2) We note that the parallel transfer coefficients to the same surface $\tau^{t,b}_{\parallel}$ are positive; this is due to the sums $a^{t,b} + b^{t,b}$ satisfying $a^{t,b} + b^{t,b} > 0$, see Figs. S2 and S3 and Secs. SIV C and SIV B in the SM [34]. This makes intuitive sense because it is natural for forces to drive velocities in the same direction when they are parallel to each other on the same surface. (3) Finally, we note that the transfer coefficient to the *opposite* surface $\tau_{\parallel}$ can be positive or negative depending on the value of $\mathbf{k}$; this is due to the sum $a + b$ satisfying $a + b < 0$, see Figs. S2 and S3 and Secs. SIV C and SIV B in the SM [34]. To elaborate on this last point, Eq. (39) indicates that $a + b < 0$ is a lower bound to $\tau_{\parallel}$ since $b < 0$; a negative lower bound on $\tau_{\parallel}$ with $a > 0$ means that the sign of $\tau_{\parallel}$ will depend on the wavevector $\mathbf{k}$. In other words, the transfer of surface force to surface velocity on the opposite side generates *velocity reversal* ($\tau_{\parallel} < 0$) for some wavevectors in which a compressional (extensional) force in the x direction on a surface can generate an extensional (compressional) velocity in the x direction on the opposite surface. For example, if $F_x(x, y) = \sin(k_x x)$, then $\tau_{\parallel} = a + b < 0$ and velocities will be reversed on the opposite surface. We discuss this in detail in the next section.

Given a driving force F_x, we show how the parallel and perpendicular transfer coefficients $\tau_{\parallel}$, $\tau_{\perp}$, $\tau^{a,b}_{\parallel}$, and $\tau^{a,b}_{\perp}$ depend on wavevector $\mathbf{k}$ of the force. Figure 4 plots $\tau_{\parallel}$ and $\tau_{\perp}$ for $h = 2\ell_0$ in which the cell height and width are roughly equal (with

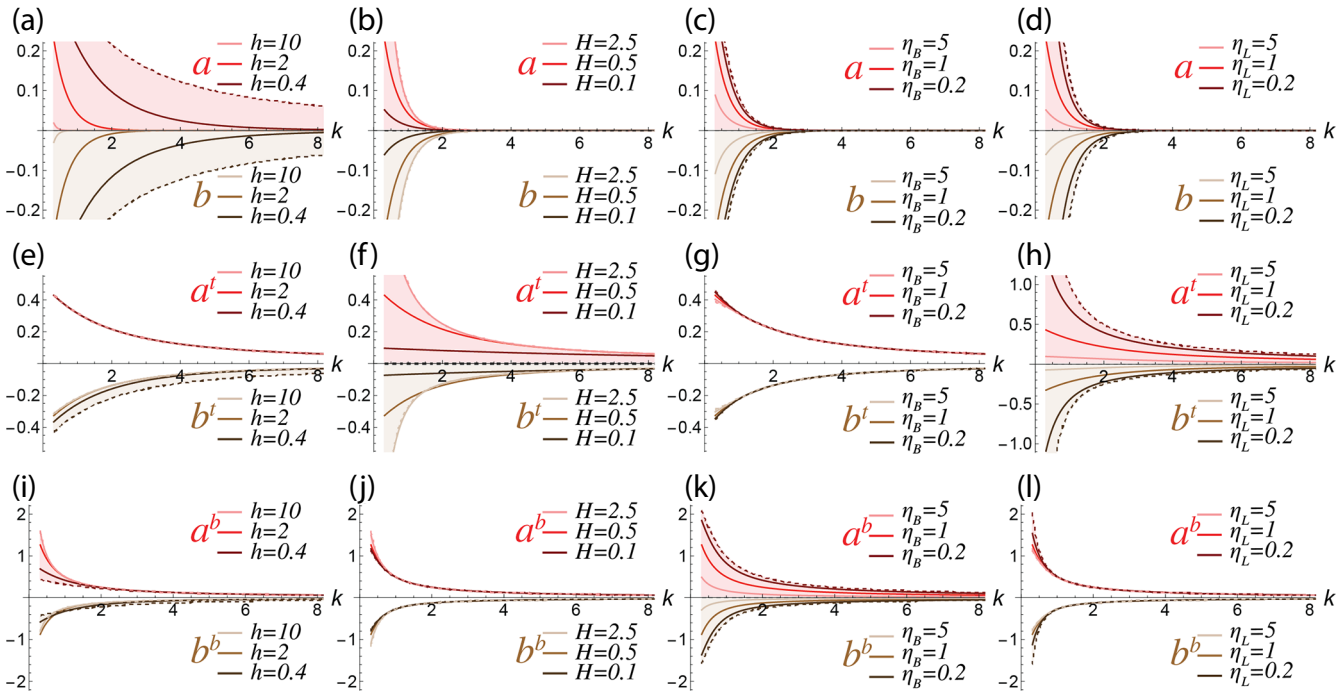

FIG. 3. Matrix elements of $\boldsymbol{\tau}$, $\boldsymbol{\tau}^{t,b}$. Quantities a, $a^{t,b}$ are graphed in red shades and quantities b, $b^{t,b}$ are graphed in brown shades as functions of k. Base parameters are $\eta = \eta_B = \eta_L = 1$, $H = 0.5$, $h = 2$, $L = 20$. Each graph varies one of these parameters and plots the result, with the shaded regions denoting the 0 to ∞ limits of each of these parameters. The 0 and ∞ limits are indicated by a dark or light dotted line, respectively. (a)–(d) $a(k)$ and $b(k)$; (e)–(h) $a^t(k)$ and $b^t(k)$; (i)–(l) $a^b(k)$ and $b^b_k(k)$.

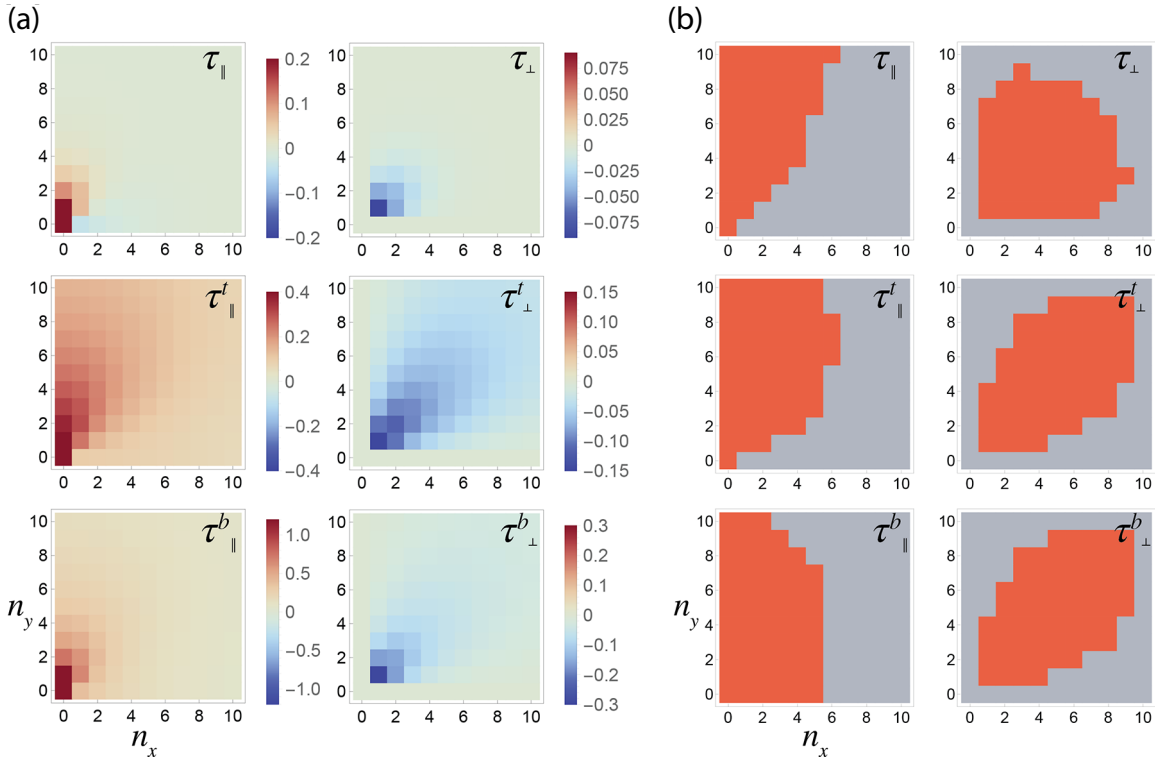

FIG. 4. Dependence of parallel and perpendicular transfer coefficients on wavevectors for $h = 2.0\ell_0$. (a) Coefficients of parallel and perpendicular transfer $\tau_\parallel$, $\tau_\perp$, $\tau^{t,b}_\parallel$, and $\tau^{t,b}_\perp$ plotted (color scale) as functions of $\mathbf{k} \equiv \frac{2\pi}{L}(n_x, n_y)$. (b) Wavevectors in which $|\tau_\parallel|$, $|\tau_\perp|$, $|\tau^{t,b}_\parallel|$, and $|\tau^{t,b}_\perp|$ are larger than their median values are highlighted in dark orange; for $\tau_\parallel$, only non-negative values greater than the median are highlighted.

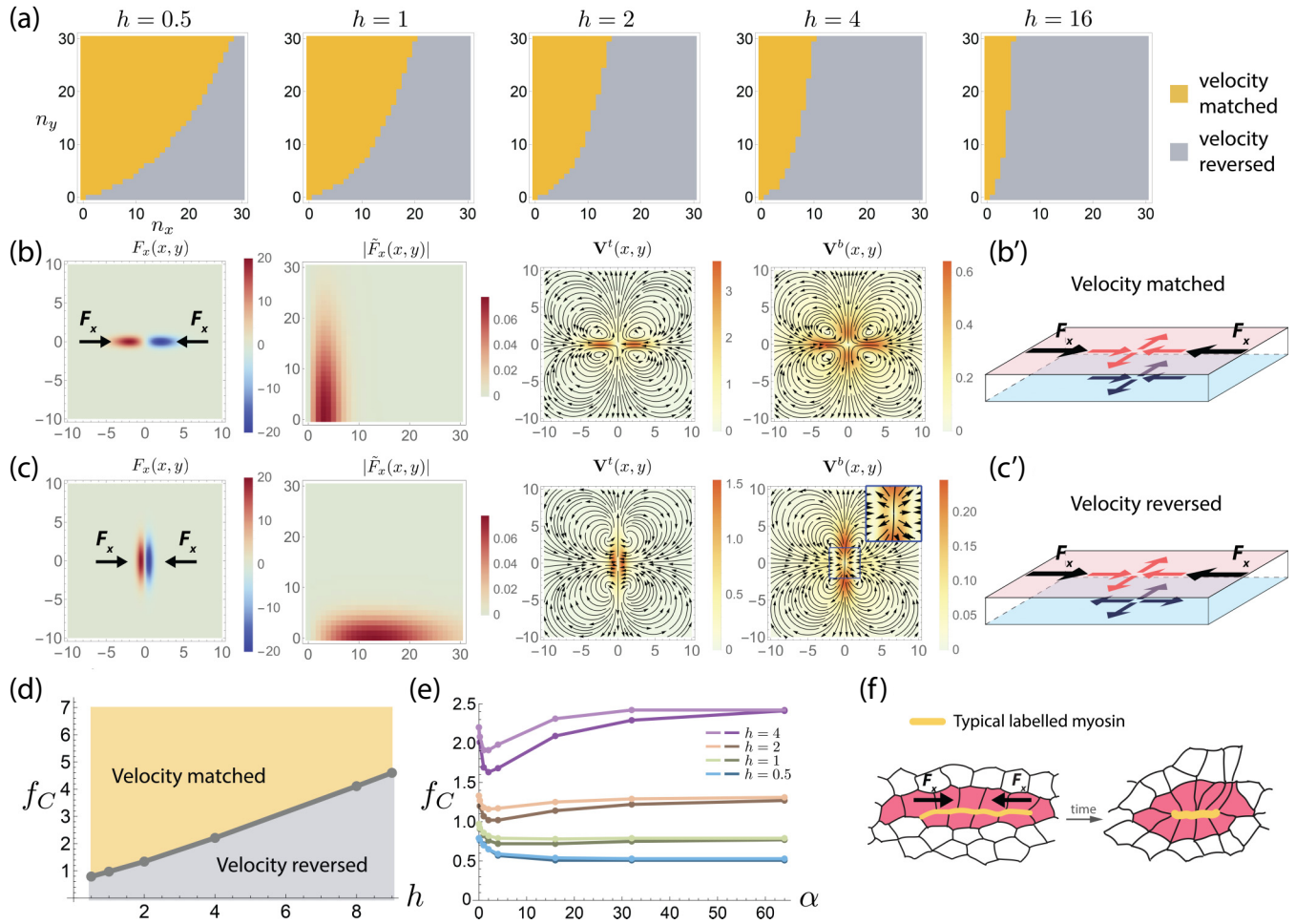

FIG. 5. Velocity matching vs velocity reversal. (a) Wavevectors that produce velocity matched (yellow) versus velocity reversed (gray) solutions for various h. As h increases, the range of $\mathbf{k}$ producing velocity matched solutions becomes smaller. (b) Velocity matching when $F_x(x, y)$ consists mainly of modes from the upper left in $\mathbf{k}$ space. (b') Schematic of velocity matching. (c) Velocity reversal when $F_x(x, y)$ consists mainly of modes from the lower right in $\mathbf{k}$ space. (c') Schematic of velocity reversal. (d) When $\alpha = 0$, with increasing h, larger f is required for velocity matched solutions; f_C is the crossover value of f. (e) Taking $\alpha > 0$, the crossover f_C for velocity matched versus velocity reversed solutions is shown for different h and A. For each h, light and dark lines indicate $A = 10$ and $A = 20$, respectively; velocity matched (reversed) solutions exist above (below) each line. F) Schematic of elongated myosin profile (interpreted as active stress profile) during convergent extension in *Drosophila*.

$\eta_{L,B} = 1, H = 0.5, L = 20$). Figures S4 and S5 (see SM [34]) show similar results for $h = 0.5$, a shorter cell, and $h = 8$, a taller cell most resembling the dimensions of a *Drosophila* cell in the ventral furrow and convergent-extension phases. First, we note that *every* perpendicular transfer is negative, confirming that compressional (extensional) forces in x always lead to extensional (compressional) forces in y as stated in point 1 above. Second, since $\tau_{\parallel}^{t,b} > 0$ everywhere, then Fig. 4 confirms point 2 above that there is never velocity reversal in the parallel direction when forces transfer to velocities on the *same* surface. And finally, considering $\tau_{\parallel}$, there exists a region in the lower right where $\tau_{\parallel} < 0$: this is the region of velocity reversal. Figure 4(b) shows that large parallel transfer coefficients are generically located in the upper left in $\mathbf{k}$ space, while large perpendicular transfer coefficients are generically located near the diagonal. Hence the modes of driving that maximize magnitudes of parallel and perpendicular transfer are different.

B. Velocity reversal when transferring to the opposite surface

If our biological problem is to find spatial profiles of driving such that top and bottom surfaces move together, then surface force modes with velocity matching ($\tau_{\parallel} > 0$) are preferred over those with velocity reversal ($\tau_{\parallel} < 0$). From Eq. (39), velocity reversal occurs whenever k_x is sufficiently close to k. Figure 5(a) shows wavevectors of the driving force that produce velocity matching and reversal: generally, wavevectors with small k_x and large k_y (the upper left in $\mathbf{k}$ space) will produce velocity matched solutions; these modes have long wavelengths in x and short wavelengths in y. If the slab thickness is increased as in Fig. 5(a), then the range of $\mathbf{k}$ that produces velocity matched solutions becomes smaller.

As an illustration of velocity reversal, consider the force profile $\mathbf{F}(x, y) = (F_x(x, y), 0)$ with

$$F_x(x, y) = -A\frac{\sqrt{e}}{f} x e^{-\frac{1}{2}(x/f)^2 - \frac{1}{2}(fy)^2} \tag{41}$$

applied to the top surface. Here f is a numerical factor controlling the profile shape. The prefactor $A\sqrt{e}/f$ is chosen such that the maximum value of F_x would be A and the integral of F_x over the half-plane $x > 0$ would have magnitude $A\sqrt{2\pi e}$, both independent of f. For $h = 1$ (with $\eta_{L,B} = 1$, $H = 0.5$, $L = 40$), Figs. 5(b) and 5(c) examine the cases $f = 2$ and $f = 0.5$, respectively. The modal content of the first case [$f = 2$ in Fig. 5(b)] sits largely in the velocity matched region of Fig. 5(a) (second panel) and indeed $\mathbf{V}^t$ and $\mathbf{V}^b$ [third and fourth panels of Fig. 5(b)] both show similar surface hyperbolic flows. Conversely, the modal content of the second case [$f = 0.5$ in Fig. 5(c)] sits primarily in the velocity reversed region, and in the third and fourth panels of Fig. 5(c), we see a transition from a hyperbolic straining surface flow in $\mathbf{V}^t$ to an outwards source-like surface flow in $\mathbf{V}^b$ near the origin.

During convergent extension of the embryonic fly epithelium, labeling has revealed elongated regions enriched in myosin ("myosin cables") aligned in the direction of convergence [6,36] [diagrammed in Fig. 5(f)]. Since these cables likely exert force profiles similar to that in Fig. 5(b), with modes largely in the velocity matched regions, we speculate that the *Drosophila* embryo may be employing a strategy of velocity matching. Since *Drosophila* tissue at this stage is very thick (around $h = 6 - 10$), large shape factors f are required to achieve velocity matching [Figs. 5(a) and 5(d)]. Indeed, a rough estimation of f from the images of myosin cables in *Drosophila* convergent extension in [5,7] yields values of $f = 3.2{-}5.3$; this is based on estimates that the length and width of myosin cables are in the range $10{-}20$ microns and $0.7{-}1.0$ microns, respectively (see details in Sec. SIV D of the SM [34]). These f values together with Fig. 5(d) indicate that these cells likely do not experience velocity reversal; however, if myosin cables were shorter, for example, 5 microns, the diameter of a single cell, then f would fall below the critical value and velocity reversal becomes likely.

To note, specific to *Drosophila* convergent extension, it is found that *both* top and bottom *active* surface forces are needed to create full convergent extension [5]. Indeed, real biological systems may involve other forces in convergent extension, not exclusively driving from a single surface. However, if the tissue utilizes surface force profiles that produce velocity matching, then this would decrease the need for additional forces. Thus it is possible that tissues (especially thick tissues), by creating long myosin cables, could be employing this strategy.

1. Dependence of velocity reversal on tissue thickness and viscoelastic strength

If we consider the tissue to be purely viscous ($\alpha = 0$), then as the tissue thickness h is increased, the value of the shape factor f from Eq. (41) needs also to be increased in order to achieve velocity matched solutions. The crossover value f_C of f between velocity matched and velocity reversed solutions is shown in Fig. 5(d).

We additionally examine how the crossover between velocity matched and velocity reversed solutions changes when the viscoelastic strength α, the tissue thickness h, and the amplitude of the driving force A are changed. Figure 5(e) shows f_C as a function of α for various values of h and A. There, values of f above (below) each line indicate force profiles creating velocity matched (reversed) solutions. We find that for large values of h, e.g., $h > 0.5$, the crossover f_C changes nonmonotonically with α, i.e., there is an optimal, middle range of α for which the velocity matched parameter region is largest. The intuition is the following: As α is increased, the tissue becomes more elastic and surfaces tend to move together, making it easier for velocity matching; on the other hand, increased elasticity also means that the material is more resistant to compression, making it harder for hyperbolic flows to appear near the origin and harder for velocity matching. Hence, intermediate values of α provide the largest velocity matched parameter regions.

C. Velocity response to periodic driving with full Oldroyd-B model

The velocity response to periodic driving in the full Stokes Oldroyd-B model is given numerically and depends on the wavevector $\mathbf{k}$ of the driving as well as on the (nondimensional) temporal driving frequency ω (units of $1/\tau_p$), proportional to the Deborah number $De \equiv \omega\tau_p/(2\pi)$. The driving force is applied to the top surface and has the form $\mathbf{F}(x, y, t) = (F_x(x, y, t), 0)$ with

$$F_x(x, y, t) = F_0 \sin(\omega t) \sin(k_x x) \sin(k_y y) \tag{42}$$

where $F_x(x, y, t) = -F_0 \sin(\omega t) \sin(k_x x)$ if $k_y = 0$ and $F_x(x, y, t) = -F_0 \sin(\omega t) \sin(k_y y)$ if $k_x = 0$.

The driving force is specified with a given wavevector (k_x, k_y) in the direction x on the top surface. However, the velocity response will consist, in general, of both x and y velocities, velocities on both surfaces, and, in particular, since $\alpha \neq 0$, velocities with components in modes other than the driving mode. In Fig. 6, we consider the component of the velocity response in the same mode as driving. In that mode, top and bottom velocities in steady-state oscillation take the form

$$\mathbf{V}^{t,b}(x, y, t) = \left(V_{0x}^{t,b} \sin\left(\omega t + \delta_x^{t,b}\right),\ V_{0y}^{t,b} \sin\left(\omega t + \delta_y^{t,b}\right)\right) \times \sin(k_x x) \sin(k_y y). \tag{43}$$

Figure 6 shows the magnitude of velocity-force responses $|V_{0x}^{t,b}/F_0|$ and $|V_{0y}^{t,b}/F_0|$ for driving wavevectors $(k_x, k_y) = \frac{2\pi}{L}(1, 0)$ [a pure compression mode, Fig. 6(a)], $(k_x, k_y) = \frac{2\pi}{L}(0, 1)$ [a pure shear mode, Fig. 6(b)], and $(k_x, k_y) = \frac{2\pi}{L}(1, 1)$ [Fig. 6(c)], simulated with $\eta_{L,B} = 1$, $h = 2$, $H = 0.5$, $L = 20$. In the pure compression and pure shear modes, the velocity response in the y direction is 0. When the viscoelastic contribution α is large enough, e.g., $\alpha = 4$ or higher in Fig. 6, the velocity response on the bottom side $|V_{0x}^b/F_0|$ and $|V_{0y}^b/F_0|$ exhibit a maximum at certain values of the Deborah number. This implies that there are certain frequencies of driving for which transfer of force to the opposite surface is optimal for the velocity modes in the same mode as the force. The angular responses $\delta_x^{t,b}$ and $\delta_y^{t,b}$ for the same driving forces are shown in Fig. S6 within the SM [34].

IV. 3D CELL DEFORMATION

A useful feature of our model is the ability to track material elements while simulating surface forces that resemble those

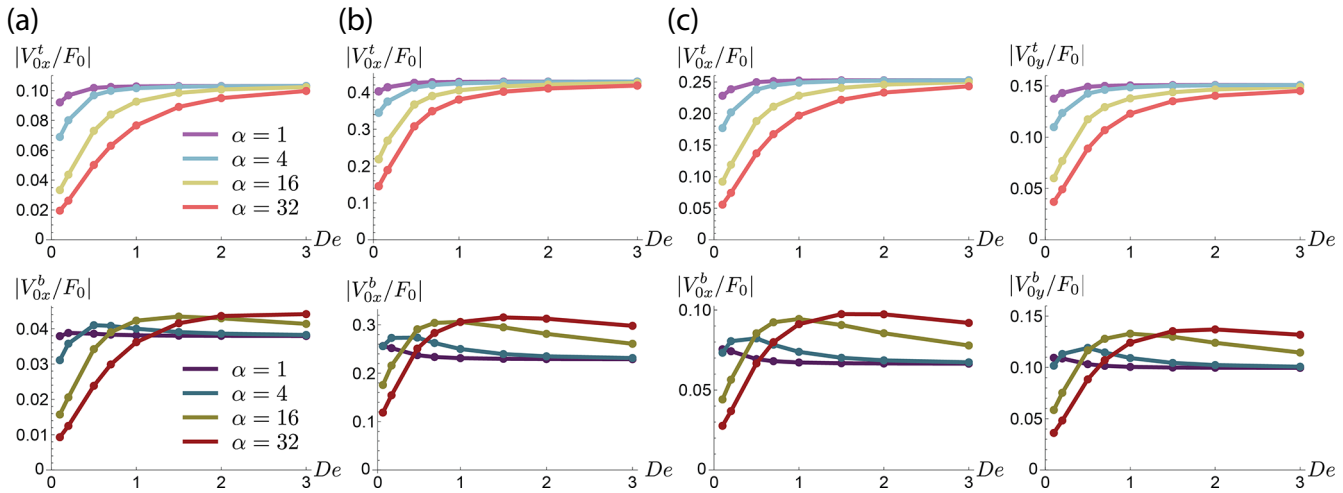

FIG. 6. Velocity response as a function of Deborah number for the driving force in Eq. (42) with (a) $(k_x, k_y) = \frac{2\pi}{L}(1, 0)$, (b) $(k_x, k_y) = \frac{2\pi}{L}(0, 1)$, and (c) $(k_x, k_y) = \frac{2\pi}{L}(1, 1)$. Color key for (b) and (c) are same as in (a).

from live experiments. If we assume that cell membranes are not force producing objects, but merely carried by the flow of the tissue material, a roughly valid assumption for very early stages of the fly embryo [28], then the movement of markers in our velocity solutions would approximate that of cell membranes. Hence, instead of modeling membranes, we track them as material surfaces. In the following, we show two examples of quantifying cell deformation dynamics using tracked membranes. Additionally, by tracking cells, we specify surface forces such that they remain localized to a particular cell as that cell moves. We find results that are suggestive in two events during *Drosophila* development: ventral furrow invagination and convergent extension.

A. Quantifying cell deformations

Figure 7 shows two illustrative examples of how cell deformation dynamics from surface forces can be simulated, quantified, and studied. In Figs. 7(a) and 7(b) and Movie S1 in the SM [34], we apply an isotropic, contractile, traveling wave force on the top surface of the tissue that moves to the right ($\eta_{L,B} = 1, h = 2, H = 0.5, L = 20$). The force is given as the divergence of the stress $\mathbf{S}(\mathbf{x}, t) = S_0 H(t) e^{-\frac{1}{2}(\frac{x-Vt}{w_x})^2 - \frac{1}{2}(\frac{y}{w_y})^2} \mathbb{1}$ where $S_0 = 20, V = 1.0, w_x = 1, w_y = 4$ (in nondimensional units) for Fig. 7(a), and $H(t)$ is a heaviside function that sets the force to zero when it has moved close to the edge of the simulation domain. Figure 7(b) shows the displacement of the origin point (0,0), tracked as a function of time, for simulations with different α ($S_0 = 20, V = 4.0$). When α is small, viscous response dominates, the total displacement is larger and shows no recoil; when α is large, elasticity plays a larger role in the response, the total displacement is smaller, and recoil from the elasticity can be observed.

In Figs. 7(c) and 7(d) and Movie S2 in the SM [34], we apply the oscillatory force in Eq. (42) with $De = 0.5, F_0 = 20$, and $\mathbf{k} = (4, 1)\frac{2\pi}{L}$ and quantify cell deformations over time. Figure 7(c) shows snapshots of deformations at the time points of: $t = 1/2$ period (top) and $t = 10$ periods (bottom) of the driving, simultaneous for all α values. For small values of α, we see that the cells are easy to deform ($\alpha = 0.1$, top) but carry no memory of past deformations ($\alpha = 0.1$, bottom) since with a low density of Oldroyd-B particles, the system is similar to a Stokes system, which is fully reversible when forcing is reversed. Meanwhile for large α, the cells are harder to deform ($\alpha = 32$, top) but carry more memory ($\alpha = 32$, bottom). And intermediate values of α show complex combinations of these limits. Figure 7(d) quantifies the change in the area of the central cell after 10 periods of oscillation when the net force integrated over time is 0. We show that depending on the Deborah number of the driving force, the maximum area deformation is achieved at different values of α.

In morphogenesis, cellular oscillations are ubiquitous; examples include cells in *Drosophila* prior to ventral furrow formation and prior to dorsal closure. Oscillations in natural systems are complex and do not result in exactly zero net force; however, we showed a simple example of periodic, zero net force driving as a case study. We found, in our example, that given 10 periods of oscillations being generated in the tissue with net zero force, there is an optimal α to create the most deformation by the end of the driving process, and this α increases when the driving frequency increases. Another insight is that tissue that is "easy to deform" (small α at $t = 1/2$ period) can be suboptimal to hold memory of the deformations if the driving reverses direction, as it regularly does in the case of stochastic forces. The two examples in Fig. 7 indicate the interesting and important role of viscoelastic strength in cell deformation dynamics and the range of cell shape phenomena that can be studied.

B. Insight into ventral furrow formation

An important event in *Drosophila* development is ventral furrow formation, occurring when a group of cells invaginate from the surface to the inside of the embryo. The invagination is preceded by many cells undergoing "pulsatile apical constriction" [4] meaning that the invaginating cells actively constrict their apical (top) surfaces in a temporally periodic manner. This process is known to be driven by myosin localized to the apical surface. After 2 to 4 cycles of apical constriction, the epithelium starts to invaginate. We model

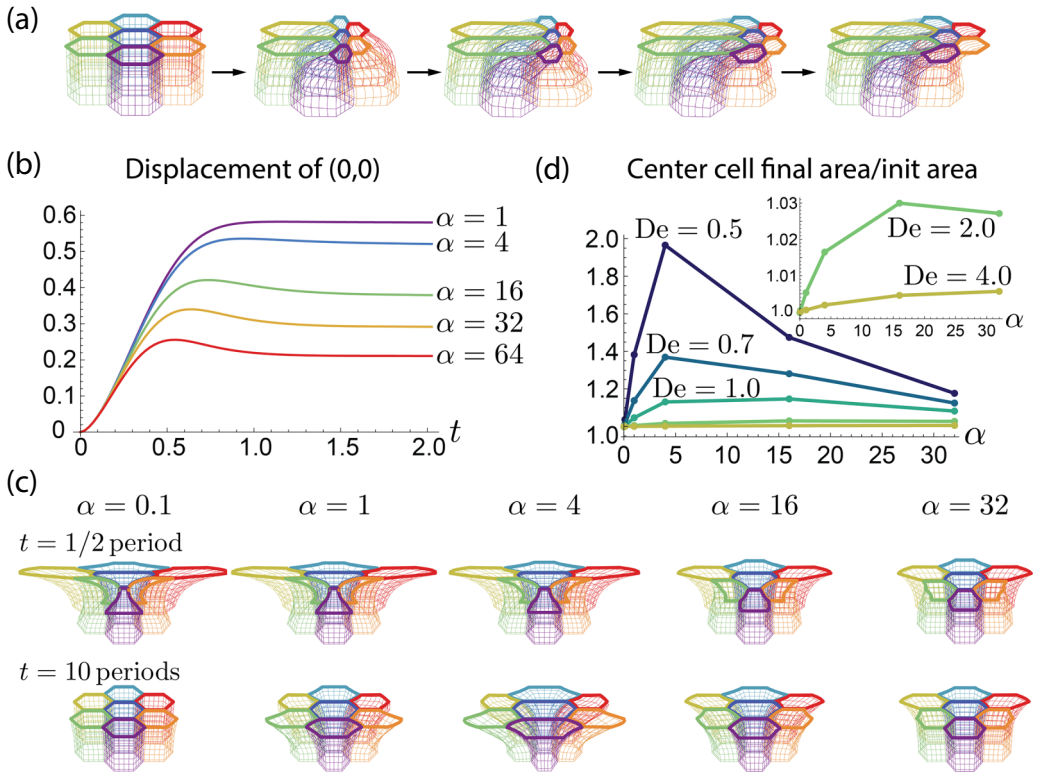

FIG. 7. Cell deformations due to surfaces forces. Depiction of cell membranes are material surfaces tracked with bulk velocity solutions. (a) Time series of cell deformations from a traveling wave contractile surface force. (b) Displacement of the origin point (0,0) tracked as a function of time for simulations with different α. (c) Cell shapes from an oscillatory force after half a period (top) and after 10 full periods (bottom) for different α. (d) Area deformation of central cell after 10 periods of oscillations; maximum deformation is achieved for different values of α depending on *De*.

these periodically constricting cells to understand the physics of invagination.

1. Estimating forces and tissue properties

To model apical constriction, we applied a local, convergent force periodically in time to a cell centered at the origin (Fig. 8(a) and Movie S3 in the SM [34]). The applied force is computed as the divergence of a 2D, isotropic, radially symmetric active stress tensor $\mathbf{S}$ whose slice at $y = 0$ is shown in Fig. 8(a). The forces from $\mathbf{S}$ model contractile forces from myosin. The tensor $\mathbf{S}$ is given by

$$\mathbf{S}(x, y, t) = \begin{pmatrix} S_{xx} & S_{xy} \\ S_{yx} & S_{yy} \end{pmatrix}, \tag{44}$$

$$S_{xy} = S_{yx} = 0, \tag{45}$$

$$S_{xx}(x, y, t) = S_{yy}(x, y, t) = -S_0 H_\omega(t) \left(\frac{r(0)}{r(t)}\right)^2 e^{-\frac{1}{2}\left(\frac{x}{r(t)}\right)^2 - \frac{1}{2}\left(\frac{y}{r(t)}\right)^2}. \tag{46}$$

This is a simple model of force feedback since $r(t)$ corresponds to the radius of the central cell as it is tracked in time. Here $r(0) = \ell_0$ is the radius of the cell at time 0 (rescaled so $\ell_0 \equiv 1$), and S_0 is the amplitude of the stress. The function $H_\omega(t)$ is a Heaviside function with $H(\omega) = 1$ when $\sin(\omega t) > 1$ and $H(\omega) = 0$ when $\sin(\omega t) < 1$, simulating the pulsatile stress being on and off at frequency ω; note that the apical constriction stress is unidirectional, it constricts or vanishes, but does not push outward. The form of $\mathbf{S}$ is chosen such that the integrals of S_{xx} and S_{yy} are constant, as $\int_\infty^\infty dxdy\, S_{xx,yy}(x, y, t) = 2\pi S_0 r(0)^2$. This simulates that the total amount of myosin in a cell's apical surface is constant in time.

During ventral furrow formation, cells undergo approximately 2.5 cycles of constriction-relaxation before the epithelium starts moving out-of-plane [4]. Therefore, our simulations of apical constriction in flat epithelial tissue can be compared to experiments for the first 2.5 simulated cycles of constriction-relaxation [dotted line in Fig. 8(c)]. Experiments in [4] estimate that cell apical areas shrink to approximately 50% their initial values during these 2.5 cycles, taking 2 to 3.5 minutes. Using that $\tau_p \approx 1$ minute [32], we simulated apical constriction in single cells using length scales relevant to *Drosophila* ($h = 8\ell_0, H = 0.5\ell_0$) with periods of forcing between $1-2\tau_p$ (corresponding to 2.5 cycles of constriction-relaxation in 2−3.5 minutes). After simulating 2.5 cycles, we identified parameters S_0 and α for which cell areas decreased to 30% to 70% (approximately 50%) their original values using $\eta_B = \eta_L = 1(\eta)$ [Fig. 8(b)].

Our simulations show that as the viscoelastic strength α is increased, the amplitude of stress must also increase to achieve the same amount of area deformation in the same time [Fig. 8(b)]; this makes sense. Since the perivitelline fluid is poorly understood, its viscosity η_L is highly uncertain. Authors of [37] have proposed that η_L could be 0.1η or lower.

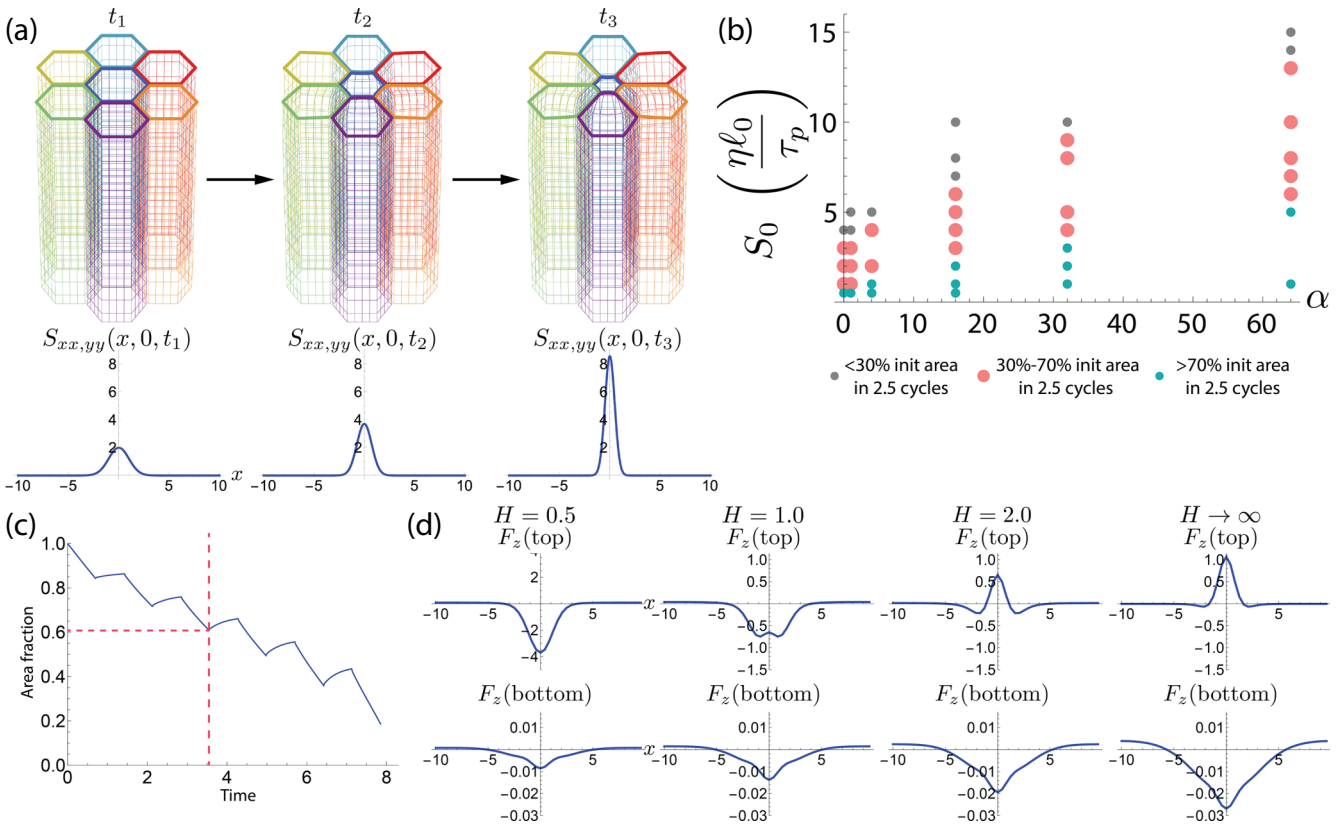

FIG. 8. Simulation of apical constriction. (a) Frames from apical constriction simulation (top); $S_{xx,yy}(x,0,t)$ at the time points of the frames. (b) Diagram of parameter space α and S_0; pink dots indicate simulations that agree with experiments. (c) Constricting cell's area as a fraction of its initial area during apical constriction simulation; dotted lines indicate 2.5 cycles of constriction-relaxation and corresponding area fraction. (d) The z-directional force F_z ($y = 0$ slice) on the tissue's top and bottom surface for various thickness of the fluid layer H. (a)–(d) parameters: $\alpha = 4$, $S_0 = 2\eta\ell_0/\tau_p$.

Hence we present parameter space estimation with $\eta_L = 0.1$ in Fig. S7 where we find that the required S_0 to fit experiments is decreased to roughly half of the $\eta_L = 1$ case.

Since dimensionless force densities are defined with units η/τ_p, then, taking η as approximately 1000 times water viscosity and $\tau_p = 60$ s, we have that 1 on the dimensionless force density scale is equivalent to $\eta/\tau_p = 1/60$ Pa. Hence, the range $S_0 = 1{-}15\,\eta\ell_0/\tau_p$ that is appropriate for various values of α [Fig. 8(b)] correspond to 2D stresses of 1/60 to 1/4 Paℓ_0, with $\ell_0 = 2{-}4$ microns.

2. *Insight into epithelial invagination*

Some models for ventral furrow invagination argued that by actively decreasing their apical areas, cells become individually wedge shaped; this shape could only be accommodated by an overall invaginated shape for the epithelium, and hence the epithelium becomes invaginated. Others argue that invagination occurs as a result of instability: a compressional force is created when cells apically constrict; the epithelium is unstable to compression and buckles. Our model elucidates the phenomena of invagination quantitatively in the context of the tissue being surrounded by incompressible fluids in three dimensions. When the active stress in Eq. (46) is applied in simulations, we calculate the force densities in the z direction exerted on the top ($z = 0$) and bottom ($z = -h$) surfaces of the tissue due to both the directly applied force and forces from its surrounding environment.

When we calculate (see Sec. SII C in the SM [34]) the z-directional forces that are exerted on the top and bottom surfaces of the tissue [$y = 0$ slices in Fig. 8(d)] for the time point at the end of the first constriction, we find that in our *Drosophila*-inspired geometry, negative z-directional forces are indeed exerted there [Fig. 8(d) left]. However, if we assume that the tissue sits in an infinite bath, that is, if we take the limit $H \to \infty$, then we see that the z force exerted on the tissue's top surface is positive, while the z force exerted on the tissue's bottom surface is negative [Fig. 8(d) right]. This means that if we eliminate the constraint that the tissue remains flat, then convergent active stresses on the tissue's surface would act to make it locally thicker instead of causing it to invaginate. If we consider intermediate cases where $H < \infty$ but is larger than its typical value in *Drosophila* [Fig. 8(d) middle panels], corresponding an enlarged space for the perivitelline fluid, then the z forces on the top and bottom surfaces of the tissue also achieve intermediate values, showing that there exists a continuum of situations between tissue invagination and tissue thickening tuned by the parameters of the surrounding fluids and boundary geometry.

Our results show that it is the presence of the hard wall (vitelline membrane) in combination with the incompressible fluid layer in region L (perivitelline fluid) that leads the

system to find a 3D solution that necessarily contains a downward force on both the tissue's top and bottom surfaces when $H = 0.5$. Intuitively, the convergent stress, because it is applied at the interface of regions L and S, drives the material in both the fluid layer and the tissue toward $(x, y) = (0, 0)$. Since these fluids are incompressible and constrained by the wall, both fluids exert a force on the other. Thus, whether or not the tissue invaginates is determined by which fluid pushes more strongly into the other. Another demonstration of this concept is in Fig. S8 (see SM [34]), in which as the viscosity of the fluid layer η_L is decreased; e.g., for $\eta_L < 0.1$, the fluid layer pushes less strongly into the tissue, and the resultant z force no longer causes the tissue to invaginate. Our explanation for invagination is different from the notion of buckling because in our case, an explicit z-directional force is produced by the competition between the fluid layer and the tissue; there is no instability.

The perivitelline space parameters that influence whether a tissue invaginates under a convergent force are the height of the perivitelline space H and the viscosity of the perivitelline fluid η_L; our model predicts that increasing the former [Fig. 8(d)] and decreasing the latter (Fig. S8 in the SM [34]) would cause the downward z-directional force on the tissue to decrease and invagination to become hindered or delayed. For our baseline values of $H = 0.5\ell_0$ and $\eta_L = \eta$ in the *Drosophila* embryo, the convergent active stress causes invagination when one cell constricts. In reality, multiple ventral furrow cells constrict as precursors to ventral furrow formation. Figure S9 in the SM [34] explores the z-directional force when the constriction is applied to a wider area of the tissue ($\approx$6 rows of cells or $8\ell_0$). When force is applied over this much larger region, the z-directional forces on the tissue's top side (apical side) point downward for a larger range of H and η_L compared to when force is applied to a single cell. A note is that authors [38] have estimated values of H as high as $H \approx 1-1.5\ell_0$ (3 microns) and η_L as low as $\eta_L = 0.001\eta$ (equivalent to water viscosity). For these estimates, our model gives that z forces point in the *opposite* direction as invagination for both single cell as well as for a wide area of constriction. This discrepancy could be due to other forces at play in a live system. Researchers may further explore our notions of precursors to invagination by finding biological systems where instead of invagination, a convergent active stress causes the tissue to locally thicken. Perhaps there are systems in which a barrier like the vitelline membrane could be removed to see whether morphogenesis proceeds differently. Additionally, one can design *in vitro* systems with controlled geometries and viscosities that test whether in-plane convergent stresses cause tissue invagination and/or thickening for various values of the parameters.

C. Convergent extension

Recent experiments have found that cells undergoing convergent-extension in both *Drosophila* [5] and vertebrates such as *Xenopus* [8,39,40] and mouse [41] exert active forces on *both* their apical and basal surfaces to create T1 transitions, a cell-level movement required for convergent extension. We simulated T1 transitions to understand whether they can be driven *exclusively* by surface forces. We used nonzero $\mathbf{F}^t$ and $\mathbf{F}^b$ that are computed as the divergence of a 2D stress tensor $\mathbf{S}$ with components,

$$S^{t,b}_{xx} = S_0 \frac{w(0)}{w(t)} e^{-\frac{1}{2}\left(\frac{x}{w^{t,b}(t)}\right)^2 - \frac{1}{2}\left(\frac{y}{w_y}\right)^2}, \quad S^{t,b}_{xy} = S^{t,b}_{yx} = S^{t,b}_{yy} = 0. \tag{47}$$

Here, $w^{t,b}(t)$ is the length of the junction executing the T1 transition (on either the top or bottom of the epithelium) as a function of time, S_0 is the amplitude of the stress, and w_y is a constant parameter that specifies a delta-like profile for the stress in the y direction; again, this is a simple model of force feedback.

Our simulations show that short cells ($h = 0.5$) are able to execute a T1 transition (Fig. 9(a) and Movie S4 in the SM [34]) throughout the height of the cells (other parameters $\eta_{L,B} = 1, H = 0.5, \alpha = 32, S_0 = 5, w_y = 0.2, L = 20$). However, tall cells, such as those in the fly embryo ($h = 8$), are not able to propagate the topological change from a T1 transition to the interior of the tissue: while both top and bottom surfaces of cells exchange neighbors, away from the surface, cells remain adjacent to their original neighbors (Fig. 9(d) and Movie S7 in the SM [34]). Even for cells that are relatively short ($h = 1, 2$, Figs. 9(b) and 9(c) and Movies S5 and S6 in the SM [34]), we see that the middle of cells cannot come together.

Another finding from our simulations is that forces at the length scales of cell junctions are required for T1 transitions (Fig. 9(e) second and fourth panels): overall force applied at the tissue-level [Fig. 9(e) third panel] cannot create T1 transitions even in very short cells ($h = 0.5$).

To note, authors in [5] showed that active forces from the basal side of the epithelium extend laterally beyond the basal surface by roughly $5-10\,\mu$m; we do not model this. However, noting that the gap between cells in Fig. 9(d) is very large, our prediction holds that for tall cells such as those in the *Drosophila* germ band, cells would require a different mechanism to execute a T1 transition through their full height. Hence, while surface forces exclusively from the apical and basal surfaces of tall epithelia are sufficient to create T1 transitions near the tissue surface, they are not sufficient to create T1 transitions for the full height of the cell, as the penetration depth of the surface force is too small. Additional forces or biological mechanisms are needed to "zip" together the remainder of the cells' lateral sides; indeed, the scutoid shapes of some epithelial cells may be indicative of incomplete T1 transitions [29,30]. The biology and mechanics of these other mechanisms may involve other molecules and are not well understood, suggesting future directions of research.

One additional point of discussion is whether membrane elasticity (which we do not model) would aid in completing the T1 transition through the full height of the tissue for tall cells such as the ones in Fig. 9(d), and do these elastic membrane forces eliminate the need for active lateral forces. The answer will depend on the elastic properties of the membrane and the height of the cells. From a rough order-of-magnitude estimate, we argue that for sufficiently *tall* cells, the force provided by membrane elasticity is not sufficient to move the bulk of the two cells in a T1 toward each other in a time that is reasonable for morphogenesis.

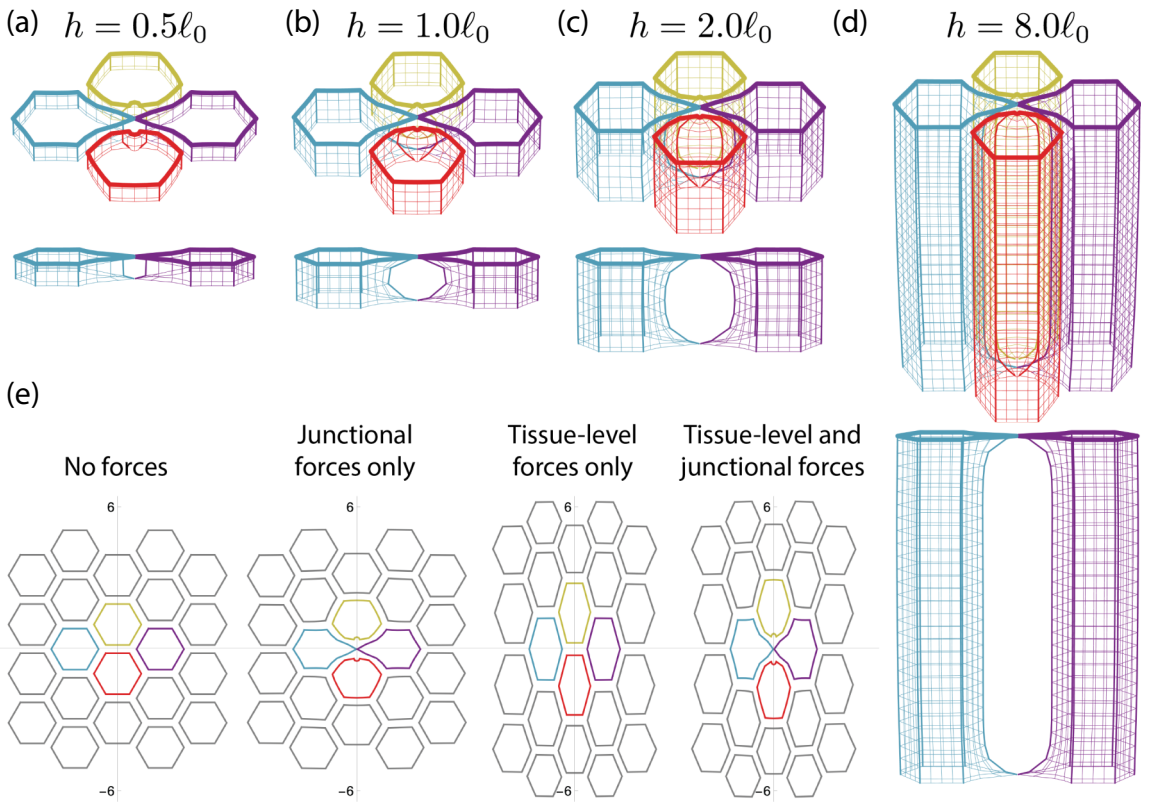

FIG. 9. Simulation of T1 transition. (a) Short cells are able to execute a T1 transition through the full height of the cell. [(b)–(d)] Cells with intermediate and large height cannot execute T1 transitions through the full height of the cell. (e) Forces on the length scales of cell junctions are required for T1 transitions. Images show apical (top surface) cell boundaries for $\mathbf{F}^t = \mathbf{F}^b = \mathbf{0}$ (first panel), $\mathbf{F}^t = \mathbf{F}^b = \nabla \cdot \mathbf{S}$ (Eq. 47) (second panel), $\mathbf{F}^t = \mathbf{F}^b = A_0(-\sin(\frac{2\pi}{L}x), \sin(\frac{2\pi}{L}y))$ (third panel), and $\mathbf{F}^t = \mathbf{F}^b = A_0(-\sin(\frac{2\pi}{L}x), \sin(\frac{2\pi}{L}y)) + \nabla \cdot \mathbf{S}$ (fourth panel).

A detailed discussion is in the Sec. SVII of the SM [34], we have an abbreviated discussion here.

Consider the situation in Fig. 9(d) in which active surface forces have moved the apical and basal sides of the cells together *up to the penetration depth of the surface force*. In this configuration, if the cell membranes were elastic, they would have stored energy in the form of bending energy and stretching energy that can then be deployed to do work to bring the two cells together. This work is roughly the drag force of the cells against the stationary fluid times the displacement required (approximately $\ell_0/2$). The reason we consider the fluid to be stationary is because the timescale of Oldroyd-B relaxation is approximately 1 minute while the timescale of the T1 is around 10–30 minutes, hence the fluid could be considered to be static at the timescale of the T1.

Balancing the stored elastic energy from the membrane and the work of the drag force requires

$$E_{\text{bend}} + E_{\text{stretch}} = F_{\text{drag}} \Delta\ell, \tag{48}$$

where E_{bend} and E_{stretch} are the energies stored in bending and stretching the membrane, respectively [see the light blue cell in Fig. 9(d) for example], F_{drag} is the drag force of the cell against the fluid, and $\Delta\ell$ is the distance the cell would travel; in this case, $\Delta\ell \approx \ell_0/2 = 2$ microns. Both E_{bend} and E_{stretch} depend linearly on their deformation moduli, κ and σ, respectively: $E_{\text{bend}} = \int dS \frac{1}{2}\kappa \frac{1}{R^2}$ and $E_{\text{stretch}} = \int dS\sigma$. Meanwhile, the drag force depends linearly on the velocity and the size of the cell R minus penetration depth R_p:

$$F_{\text{drag}} = 6\pi V \eta (R - R_p) \cdot G(\epsilon) \cdot L_u. \tag{49}$$

Here, $R - R_p$ denotes the radius of the object that is being dragged (the part of the cell that has not been moved by the surface force). The velocity can be set to $V = \frac{\text{length to travel}}{\text{time to travel}} = \frac{\ell_0/2}{T}$ with T denoting the time to travel. Viscosity is approximately $\eta = 1\frac{N}{m^2}s$ for cytoskeleton. The factor $G(\epsilon)$ is a geometric parameter depending on the ellipticity ϵ that accounts for the fact that the cell is not a sphere, this will depend on the shape of the cell, however, it is on the order of 1. Finally, lubrication L_u is a parameter that accounts for the fact that we are not pushing a cell through infinite fluid, instead, we are pushing it towards another cell, which is quite close, meaning that the drag force is increased; the lubrication parameter could contribute a factor of approximately 2 to 10 (see [42]). Altogether, the balance of membrane elasticity and drag is approximately

$$\int dS \frac{\kappa}{2}\frac{1}{R^2} + \int dS\sigma = 6\pi \frac{\ell_0/2}{T}\left(1\frac{N}{m^2}s\right)(R - R_p) \cdot G(\epsilon) \cdot L_u. \tag{50}$$

Solving for time to travel T, we have

$$T = \frac{6\pi \ell_0/2\left(1\frac{N}{m^2}s\right)(R - R_p) \cdot G(\epsilon) \cdot L_u}{\int dS \frac{\kappa}{2}\frac{1}{R^2} + \int dS\sigma}. \tag{51}$$

This expression estimates the time that it would take for membrane elasticity to move the cells closer together. For the geometry in Fig. 9(d) with estimates of $\kappa = 20k_BT$ and $\sigma = 1.7 \times 10^{-8}\frac{N}{m}$ from [43], we have that the time to travel is $T \approx 156 \cdot L_u \cdot$ minutes (see Sec. SVII in the SM [34]), with lubrication representing a factor of ≈ 2 to 10; this is too long compared to the timescale of a typical T1 transition. Hence, we hypothesize that *active lateral forces are needed in addition to membrane elasticity for tall cells* like those in *Drosophila* to complete T1 transitions.

In addition, consider how in Eq. (51), the time to travel is decreased if parameters κ and σ are increased, and it is also decreased if the (half-)height of the cell R is decreased. Hence for larger values of the membrane elasticity moduli and *shorter* cells (perhaps Fig. 9(b), discussed in Sec. SVII of the SM [34]), we hypothesize that there are scenarios in which only membrane elasticity and surface forces are required to complete the T1 transition through the full height of the tissue, even though active lateral forces will be required for taller cells.

V. DISCUSSION

We addressed a need for 3D modeling in thick epithelial tissues. In particular, 2D epithelial models cannot give insight to morphogenetic processes in which the apical and basal sides of cells do not move in concert. Here, we provided a framework for modeling flat, viscoelastic tissue that takes into account tissue thickness as an important parameter. We presented analytical and numerical solutions to the system, and our mathematical framework will allow us to eventually evolve active stresses as surface populations in future extensions of the model.

We analyzed how applied surfaces forces drive surface velocities by studying transfer matrices. A key result of our analysis is the existence of velocity matched versus velocity reversed solutions on the side of the tissue opposite from the force. We found that to achieve velocity matched solutions, the modal composition of the driving force should be heavily weighed with long wavelength wavevectors in the direction parallel to the force (small k_x) and short wavelength wavevectors in the direction perpendicular to the force (large k_y). This pattern of driving is seen in the *Drosophila* germ band during convergent extension where authors observe "myosin cables" [6,36]. This result hints that the *Drosophila* germ band may be employing (in addition to basal forces) a strategy of velocity matching to help cells move their apical and basal surfaces in concert as much as possible across a thick epithelium.

Because our model of epithelial tissue is fully immersed in a realistic fluid environment, we are able to calculate the forces induced by other parts of the system on the epithelium when active stresses are applied. In simulations of apical constriction, we showed that when an active constricting force is applied parallel to the surface (in x and y), an orthogonal, z-directional force is induced on the tissue surface from adjacent fluids; and this is the force that ultimately will cause invagination in our model (as we do not model other forces). The direction and amplitude of this force depends strongly on the presence and parameters of other fluids in the system and on geometric constraints. Hence, our paper suggests that future studies of morphogenesis should include analysis of how geometric constraints and fluid surroundings influence the shapes of tissues.

Using apical constriction simulations, we estimated the amplitude of surface stress created by medial myosin. These estimates are only the starting point because our simulations assumed that viscosity and viscoelastic strength are spatially constant throughout the tissue. Authors of [33] have shown that cells are in fact spatially heterogeneous in viscosity and viscoelastic strength even within the same cell. An elaboration of our model would be to take α and η to be space-dependent and/or to specify an evolving field $\phi(\mathbf{x}, t)$ corresponding to the density of viscoelastic polymers in the tissue.

One key assumption in our model is that lateral membranes are not force-generating objects. In this paper, we took advantage of the fact that this assumption is roughly valid in the early *Drosophila* embryo [28] to model events during embryogenesis. However, since others have shown that there are actomyosin forces localized to lateral membranes during EMT [44], apoptosis [45], and the start of convergent-extension in the *Drosophila* mesoderm [46], a future direction will be to take into account forces from lateral membranes that may be contributing to bulk mechanics. We here showed that forces from lateral membranes likely play a role during T1 transitions in tall cells such as those in *Drosophila*. We showed that the transfer of surface force to velocities in the tissue interior is so low, that without forces from the lateral sides of cells, T1 transitions cannot propagate through the full height of the cell, and hence additional forces, perhaps due to molecules like cadherens, are required. This is another direction of future work.

Finally, a promising direction of our work is to rigorously evolve a population of active force generators on our tissue surface alongside the bulk material. In our mathematical framework, we have the potential to incorporate any 2D active population into our system and ask: How can these populations remodel the epithelium in 3D, and how does the motion of epithelial cells couple back to the active population? Active populations include surface actomyosin, but also collections of bacteria, or a 2D model of active cellular apical surfaces and elastic membranes; our framework can evolve these populations consistently with how the tissue and other fluids move in 3D. These populations might couple to reaction-diffusion equations such as those specifying chemical oscillations, trigger waves, or genetic circuits. For example, calcium is a molecule that transports into cells under mechanical tension and feeds back to cytoskeletal forces [47,48]: our model can simulate cellular calcium concentrations and alter material parameters locally. The coupling between 2D active populations and 3D tissue will not only provide opportunities to study rich mathematical structures in these systems but also provide quantitative model predictions to connect to experiments in a wide variety of settings that involve tissues, fluid environments, and boundaries.

[1] M. Osterfield, XinXin Du, T. Schüpbach, E. Wieschaus, and S. Y. Shvartsman, Three-dimensional epithelial morphogenesis in the developing *Drosophila* egg, Dev. Cell **24**, 400 (2013).

[2] M. Leptin and B. Grunewald, Cell shape changes during gastrulation in *Drosophila*, Development **110**, 73 (1990).

[3] D. Sweeton, S. Parks, M. Costa, and E. Wieschaus, Gastrulation in *Drosophila*: The formation of the ventral furrow and posterior midgut invaginations, Development **112**, 775 (1991).

[4] A. C. Martin, M. Kaschube, and E. F. Wieschaus, Pulsed contractions of an actin–myosin network drive apical constriction, Nature (London) **457**, 495 (2009).

[5] Z. Sun, C. Amourda, M. Shagirov, Y. Hara, T. E. Saunders, and Y. Toyama, Basolateral protrusion and apical contraction cooperatively drive *Drosophila* germ-band extension, Nat. Cell Biol. **19**, 375 (2017).

[6] J. A. Zallen and E. Wieschaus, Patterned gene expression directs bipolar planar polarity in *Drosophila*, Dev. Cell **6**, 343 (2004).

[7] J. T. Blankenship, S. T. Backovic, J. S. P. Sanny, O. Weitz, and J. A. Zallen, Multicellular rosette formation links planar cell polarity to tissue morphogenesis, Dev. Cell **11**, 459 (2006).

[8] S. Weng, R. J. Huebner, and J. B. Wallingford, Convergent extension requires adhesion-dependent biomechanical integration of cell crawling and junction contraction, Cell Rep. **39**, 110666 (2022).

[9] N. Founounou, R. Farhadifar, G. M. Collu, U. Weber, M. J. Shelley, and M. Mlodzik, Tissue fluidity mediated by adherens junction dynamics promotes planar cell polarity-driven ommatidial rotation, Nat. Commun. **12**, 6974 (2021).

[10] R. Farhadifar, J.-C. Röper, B. Aigouy, S. Eaton, and F. Jülicher, The influence of cell mechanics, cell-cell interactions, and proliferation on epithelial packing, Curr. Biol. **17**, 2095 (2007).

[11] H. Honda, Geometrical models for cells in tissues, Int. Rev. Cytol. **81**, 191 (1983).

[12] T. Nagai, K. Kawasaki, and K. Nakamura, Vertex dynamics of two-dimensional cellular patterns, J. Phys. Soc. Jpn. **57**, 2221 (1988).

[13] T. Nagai and H. Honda, A dynamic cell model for the formation of epithelial tissues, Philos. Mag. B **81**, 699 (2001).

[14] A. G. Fletcher, M. Osterfield, R. E. Baker, and S. Y. Shvartsman, Vertex models of epithelial morphogenesis, Biophys. J. **106**, 2291 (2014).

[15] D. Drasdo, R. Kree, and J. S. McCaskill, Monte Carlo approach to tissue-cell populations, Phys. Rev. E **52**, 6635 (1995).

[16] M. Basan, J. Elgeti, E. Hannezo, W.-J. Rappel, and H. Levine, Alignment of cellular motility forces with tissue flow as a mechanism for efficient wound healing, Proc. Natl. Acad. Sci. USA **110**, 2452 (2013).

[17] H. Honda, M. Tanemura, and T. Nagai, A three-dimensional vertex dynamics cell model of space-filling polyhedra simulating cell behavior in a cell aggregate, J. Theor. Biol. **226**, 439 (2004).

[18] M. Misra, B. Audoly, I. G. Kevrekidis, and S. Y. Shvartsman, Shape transformations of epithelial shells, Biophys. J. **110**, 1670 (2016).

[19] C. Bielmeier, S. Alt, V. Weichselberger, M. La Fortezza, H. Harz, F. Jülicher, G. Salbreux, and A.-K. Classen, Interface contractility between differently fated cells drives cell elimination and cyst formation, Curr. Biol. **26**, 563 (2016).

[20] E. Hannezo, J. Prost, and J.-F. Joanny, Theory of epithelial sheet morphology in three dimensions, Proc. Natl. Acad. Sci. USA **111**, 27 (2014).

[21] S. Okuda, N. Takata, Y. Hasegawa, M. Kawada, Y. Inoue, T. Adachi,Y. Sasai, and M. Eiraku, Strain-triggered mechanical feedback in self-organizing optic-cup morphogenesis, Sci. Adv. **4**, eaau1354 (2018).

[22] S. Okuda and K. Fujimoto, A mechanical instability in planar epithelial monolayers leads to cell extrusion, Biophys. J. **118**, 2549 (2020).

[23] V. Conte, J. J. Muñoz, and M. Miodownik, A 3d finite element model of ventral furrow invagination in the *Drosophilamelanogaster* embryo, J. Mech. Behav. Biomed. Mater. **1**, 188 (2008).

[24] N. C. Heer, P. W. Miller, S. Chanet, N. Stoop, J. Dunkel, and A. C. Martin, Actomyosin-based tissue folding requires a multicellular myosin gradient, Development **144**, 4249 (2017).

[25] H. G. Yevick, P. W. Miller, J. Dunkel, and A. C. Martin, Structural redundancy in supracellular actomyosin networks enables robust tissue folding, Dev. Cell **50**, 586 (2019).

[26] H. Berthoumieux, J.-L. Maître, C.-P. Heisenberg, E. K. Paluch, F. Jülicher, and G. Salbreux, Active elastic thin shell theory for cellular deformations, New J. Phys. **16**, 065005 (2014).

[27] H. B. da Rocha, J. Bleyer, and H. Turlier, A viscous active shell theory of the cell cortex, J. Mech. Phys. Solids **164**, 104876 (2022).

[28] B. He, K. Doubrovinski, O. Polyakov, and E. Wieschaus, Apical constriction drives tissue-scale hydrodynamic flow to mediate cell elongation, Nature (London) **508**, 392 (2014).

[29] J.-F. Rupprecht, K. Haur Ong, J. Yin, A. Huang, H.-H.-Q. Dinh, A. P. Singh, S. Zhang, W. Yu, and T. E. Saunders, Geometric constraints alter cell arrangements within curved epithelial tissues, Mol. Biol. Cell **28**, 3582 (2017).

[30] P. Gómez-Gálvez, P. Vicente-Munuera, A. Tagua, C. Forja, A. M. Castro, M. Letrán, A. Valencia-Expósito, C. Grima, M. Bermúdez-Gallardo, Ó. Serrano-Pérez-Higueras *et al.*, Scutoids are a geometrical solution to three-dimensional packing of epithelia, Nat. Commun. **9**, 2960 (2018).

[31] G. Forgacs, R. A. Foty, Y. Shafrir, and M. S. Steinberg, Viscoelastic properties of living embryonic tissues: A quantitative study, Biophys. J. **74**, 2227 (1998).

[32] K. Doubrovinski, M. Swan, O. Polyakov, and E. F. Wieschaus, Measurement of cortical elasticity in *Drosophila melanogaster* embryos using ferrofluids, Proc. Natl. Acad. Sci. USA **114**, 1051 (2017).

[33] A. D. Wessel, M. Gumalla, J. Grosshans, and C. F. Schmidt, The mechanical properties of early *Drosophila* embryos measured by high-speed video microrheology, Biophys. J. **108**, 1899 (2015).

[34] See Supplemental Material at http://link.aps.org/supplemental/10.1103/PhysRevResearch.5.023190 for details of mathematical derivations and to elaborate on points of discussion.

[35] H. Masoud and M. J. Shelley, Collective Surfing of Chemically Active Particles, Phys. Rev. Lett. **112**, 128304 (2014).

[36] C. Bertet, L. Sulak, and T. Lecuit, Myosin-dependent junction remodelling controls planar cell intercalation and axis elongation, Nature (London) **429**, 667 (2004).

[37] A. N. Goldner and K. Doubrovinski, What basal membranes can tell us about viscous forces in *Drosophila* ventral furrow formation, *bioRxiv* 2021.04.21.440835 (2021), doi:10.1101/2021.04.21.440835.

[38] M. I. Cheikh, J. Tchoufag, K. Dean, S. Bhaduri, Z. Chuzhong, K. K. Mandadapu, and K. Doubrovinski, Cantilever-based in vivo measurements in the early *Drosophila* embryo reveal adiabatic elastic response on developmentally relevant time scales, *bioRxiv* 2022.08.12.503803 (2022), doi:10.1101/2022.08.12.503803.

[39] R. J. Huebner and J. B. Wallingford, Coming to consensus: A unifying model emerges for convergent extension, Dev. Cell **46**, 389 (2018).

[40] J. Shih and R. Keller, Cell motility driving mediolateral intercalation in explants of *Xenopus laevis*, Development **116**, 901 (1992).

[41] M. Williams, W. Yen, X. Lu, and A. Sutherland, Distinct apical and basolateral mechanisms drive planar cell polarity-dependent convergent extension of the mouse neural plate, Dev. Cell **29**, 34 (2014).

[42] G. K. Batchelor, *An Introduction to Fluid Dynamics* (Cambridge University Press, Cambridge, 2000).

[43] S. A. Rautu, D. Orsi, L. Di Michele, G. Rowlands, P. Cicuta, and M. S. Turner, The role of optical projection in the analysis of membrane fluctuations, Soft Matter **13**, 3480 (2017).

[44] M. Gracia, S. Theis, A. Proag, G. Gay, C. Benassayag, and M. Suzanne, Mechanical impact of epithelial- mesenchymal transition on epithelial morphogenesis in *Drosophila*, Nat. Commun. **10**, 1 (2019).

[45] B. Monier, M. Gettings, G. Gay, T. Mangeat, S. Schott, A. Guarner, and M. Suzanne, Apico-basal forces exerted by apoptotic cells drive epithelium folding, Nature (London) **518**, 245 (2015).

[46] A. John and M. Rauzi, A two-tier junctional mechanism drives simultaneous tissue folding and extension, Dev. Cell **56**, 1469 (2021).

[47] G. L. Hunter, J. M. Crawford, J. Z. Genkins, and D. P. Kiehart, Ion channels contribute to the regulation of cell sheet forces during *Drosophila* dorsal closure, Development **141**, 325 (2014).

[48] N. Christodoulou and P. A. Skourides, Cell-autonomous Ca^{2+} flashes elicit pulsed contractions of an apical actin network to drive apical constriction during neural tube closure, Cell Rep. **13**, 2189 (2015).